Monthly Notices
of the
ROYAL ASTRONOMICAL SOCIETY

MNRAS **434,** 3218–3235 (2013)
Advance Access publication 2013 August 8

doi:10.1093/mnras/stt1258

Herschel reveals the obscured star formation in HiZELS Hα emitters at $z = 1.47$

E. Ibar,[1,2⋆] D. Sobral,[3] P. N. Best,[4] R. J. Ivison,[1,4] I. Smail,[5] V. Arumugam,[4] S. Berta,[6] M. Béthermin,[7,8] J. Bock,[9,10] A. Cava,[11] A. Conley,[12] D. Farrah,[13] J. Geach,[14] S. Ikarashi,[15] K. Kohno,[15,16] E. Le Floc'h,[7] D. Lutz,[6] G. Magdis,[7] B. Magnelli,[6] G. Marsden,[17] S. J. Oliver,[13] M. J. Page,[18] F. Pozzi,[19] L. Riguccini,[7] B. Schulz,[9,20] N. Seymour,[18,21] A. J. Smith,[13] M. Symeonidis,[18] L. Wang,[5,13] J. Wardlow[22] and M. Zemcov[9,10]

[1] *UK Astronomy Technology Centre, Science and Technology Facilities Council, Royal Observatory, Blackford Hill, Edinburgh EH9 3HJ, UK*
[2] *Instituto de Astrofísica, Facultad de Física, Pontificia Universidad Católica de Chile, Casilla 306, Santiago 22, Chile*
[3] *Leiden Observatory, Leiden University, PO Box 9513, NL-2300 RA Leiden, the Netherlands*
[4] *Institute for Astronomy, University of Edinburgh, Royal Observatory, Blackford Hill, Edinburgh EH9 3HJ, UK*
[5] *Institute for Computational Cosmology, Durham University, South Road, Durham DH1 3LE, UK*
[6] *Max-Planck-Institut für Extraterrestrische Physik (MPE), Postfach 1312, D-85741 Garching, Germany*
[7] *Laboratoire AIM-Paris-Saclay, CEA/DSM/Irfu – CNRS – Université Paris Diderot, CE-Saclay, pt courrier 131, F-91191 Gif-sur-Yvette, France*
[8] *Institut d'Astrophysique Spatiale (IAS), bâtiment 121, Université Paris-Sud 11 and CNRS (UMR 8617), F-91405 Orsay, France*
[9] *California Institute of Technology, 1200 E. California Blvd., Pasadena, CA 91125, USA*
[10] *Jet Propulsion Laboratory, 4800 Oak Grove Drive, Pasadena, CA 91109, USA*
[11] *Departamento de Astrofísica, Facultad de CC. Físicas, Universidad Complutense de Madrid, E-28040 Madrid, Spain*
[12] *Center for Astrophysics and Space Astronomy 389-UCB, University of Colorado, Boulder, CO 80309, USA*
[13] *Astronomy Centre, Department of Physics & Astronomy, University of Sussex, Brighton BN1 9QH, UK*
[14] *Centre for Astrophysics Research, University of Hertfordshire, College Lane, Hatfield, Hertfordshire AL10 9AB, UK*
[15] *Institute of Astronomy, University of Tokyo, 2-21-1 Osawa, Mitaka, Tokyo 181-0015, Japan*
[16] *Research Center for the Early Universe, University of Tokyo, 7-3-1 Hongo, Bunkyo, Tokyo 113-0033, Japan*
[17] *Department of Physics & Astronomy, University of British Columbia, 6224 Agricultural Road, Vancouver, BC V6T 1Z1, Canada*
[18] *Mullard Space Science Laboratory, University College London, Holmbury St. Mary, Dorking, Surrey RH5 6NT, UK*
[19] *INAF–Osservatorio Astronomico di Roma, via di Frascati 33, I-00040 Monte Porzio Catone, Italy*
[20] *Infrared Processing and Analysis Center, MS 100-22, California Institute of Technology, JPL, Pasadena, CA 91125, USA*
[21] *CSIRO Astronomy & Space Science, PO Box 76, Epping, NSW 1710, Australia*
[22] *Department of Physics & Astronomy, University of California, Irvine, CA 92697, USA*

Accepted 2013 July 4. Received 2013 July 3; in original form 2012 November 30

ABSTRACT

We describe the far-infrared (far-IR; rest-frame 8–1000-μm) properties of a sample of 443 Hα-selected star-forming galaxies in the Cosmic Evolution Survey (COSMOS) and Ultra Deep Survey (UDS) fields detected by the High-redshift Emission Line Survey (HiZELS) imaging survey. Sources are identified using narrow-band filters in combination with broad-band photometry to uniformly select Hα (and [O II] if available) emitters in a narrow redshift slice at $z = 1.47 \pm 0.02$. We use a stacking approach in *Spitzer*-MIPS mid-IR, *Herschel*-PACS/SPIRE far-IR [from the PACS Evolutionary Prove (PEP) and Herschel Multi-tiered Extragalactic Survey (HerMES)] and AzTEC mm-wave images to describe their typical far-IR properties. We find that HiZELS galaxies with observed Hα luminosities of $L(\mathrm{H}\alpha)_{\mathrm{obs}} \approx 10^{8.1-9.1}$ L$_\odot$ ($\approx 10^{41.7-42.7}$ erg s^{-1}) have bolometric far-IR luminosities of typical luminous IR galaxies, $L(8-1000\,\mu\mathrm{m}) \approx 10^{11.41^{+0.04}_{-0.06}}$ L$_\odot$. Combining the Hα and far-IR luminosities, we derive median star formation rates (SFRs) of $\mathrm{SFR}_{\mathrm{H}\alpha,\,\mathrm{FIR}} = 32 \pm 5$ M$_\odot$ yr^{-1} and Hα extinctions of $A_{\mathrm{H}\alpha} = 1.0 \pm 0.2$ mag. Perhaps surprisingly, little difference is seen in typical HiZELS

⋆ E-mail: edoibar.puc@gmail.com

extinction levels compared to local star-forming galaxies. We confirm previous empirical stellar mass (M_*) to $A_{\rm H\alpha}$ relations and the little or no evolution up to $z = 1.47$. For HiZELS galaxies (or similar samples) we provide an empirical parametrization of the SFR as a function of rest-frame $(u - z)$ colours and 3.6-μm photometry – a useful proxy to aid in the absence of far-IR detections in high-z galaxies. We find that the observed Hα luminosity is a dominant SFR tracer when rest-frame $(u - z)$ colours are $\lesssim$0.9 mag or when *Spitzer*-3.6-μm photometry is fainter than 22 mag (Vega) or when stellar masses are lower than $10^{9.7}$ M$_\odot$. We do not find any correlation between the [O II]/Hα and far-IR luminosity, suggesting that this emission line ratio does not trace the extinction of the most obscured star-forming regions, especially in massive galaxies where these dominate. The luminosity-limited HiZELS sample tends to lie above of the so-called main sequence for star-forming galaxies, especially at low stellar masses, indicating high star formation efficiencies in these galaxies. This work has implications for SFR indicators and suggests that obscured star formation is linked to the assembly of stellar mass, with deeper potential wells in massive galaxies providing dense, heavily obscured environments in which stars can form rapidly.

Key words: galaxies: high-redshift – galaxies: starburst – galaxies: star formation – galaxies: statistics – infrared: galaxies – submillimetre: galaxies.

1 INTRODUCTION

Historically, the classical star formation rate (SFR) indicator has been Hα ($\lambda_{\rm rest} = 656.3$ nm) luminosity – a well-calibrated probe of instantaneous emission from massive, young stars (<20 Myr and >8 M$_\odot$; e.g. Kennicutt 1998). To extrapolate the observed starlight from O and B stars to the total SFR requires careful consideration of the initial mass function (IMF) of the stellar population and the amount of extinction (scattering and absorption by dust) suffered by the starlight. Discrepancies of up to ∼30 per cent can be found amongst previously published Hα-based SFR calibrations, due mainly to the use of different models of stellar evolution and stellar atmospheres.

Of all the assumptions required to convert observed quantities into SFRs, the main limitation is the sensitivity of Hα flux to extinction [$A_{\rm H\alpha}$, where the intrinsic Hα luminosity is defined as $L({\rm H}\alpha)_{\rm int} = L({\rm H}\alpha)_{\rm obs} \times 10^{0.4\,A_{\rm H\alpha}}$]. The observed line fluxes represent only a fraction of the intrinsic emission, with typical values of $A_{\rm H\alpha}$ found to be ≈0.8–1.1 mag in optically selected samples (Niklas, Klein & Wielebinski 1997; Sobral et al. 2012). In general, when the level of extinction is low or moderate, $A_{\rm H\alpha} \lesssim 3$ mag, the difference between the observed Balmer decrement (Hα/Hβ; e.g. see Calzetti 2001) and the theoretical expectation (2.86 for Case B recombination: electron temperature $T_{\rm e} = 10^4$ K and density $n_{\rm e} = 10^2$ cm^{-3}; Brocklehurst 1971; Kennicutt 1998) can be used to determine the amount of extinction (assuming a model for the wavelength-dependence of the attenuation; e.g. Fischera & Dopita 2005) as this Hα/Hβ ratio scales directly with the total ionizing flux of the embedded stars. Unfortunately, the combination of extinction and increasing redshift make detection of Hydrogen lines difficult (especially for Hβ, $\lambda_{\rm rest} = 486.1$ nm). Indeed, to study star formation processes via conventional means at high redshift is a major challenge (e.g. Dominguez et al. 2013; Stott et al. 2013).

A way to measure the SFR at high redshift is by considering that the UV/optical photons that are absorbed by the surrounding media are re-emitted in the far-infrared (far-IR) waveband (e.g. Heinis et al. 2013), meaning that far-IR observables can be used as a tracer of the obscured SFR and/or the amount of extinction in a galaxy. For example, if all the starlight is absorbed then the system works as a calorimeter and the far-IR becomes the ideal tracer of SFR (Lacki, Thompson & Quataert 2010). This measure includes those contributions from heavily obscured star formation and those from old stellar populations (e.g. Salim et al. 2009). These far-IR SFR estimates have an intimate relationship with the level of extinction suffered by the starlight. We stress that we think of extinction as an average quantity measured towards all star-forming regions of a galaxy, and it therefore presents several other intricate dependences, e.g. on geometry, luminosity, mass, environment, radiation fields, etc. (e.g. Dutton, van den Bosch & Dekel 2010).

A previous study in the local Universe, $\langle z \rangle \approx 0.08$, by Garn & Best (2010), using data from the Sloan Digital Sky Survey (SDSS; York et al. 2000), showed that one of the strongest parameters correlating with the level of extinction in galaxies is stellar mass, M_* (see also Brinchmann et al. 2004; Gilbank et al. 2010; Wuyts et al. 2011). These studies suggest that the level of extinction produced by the material in and surrounding their star-forming regions increase as the galaxies built up their stellar mass. Using Hα- and H-band selected galaxies, Sobral et al. (2012) and Hilton et al. (2012) find that this behaviour seems to hold even at $z \approx 1.5$–3. On the other hand, various studies have shown that mass plays a key role in driving the amount of star formation (e.g. at $z \sim 1.5$; see Daddi et al. 2007; Elbaz et al. 2007; Noeske et al. 2007; Pannella et al. 2009), where the SFR is found to be roughly linearly correlated to the stellar mass and defines a typical value for the specific star formation rate (sSFR = SFR/M_*), where more violent star formation is seen in more massive galaxies.

Using data from the *Herschel Space Observatory*[1] (Pilbratt et al. 2010), Elbaz et al. (2011) propose, somewhat controversially, the existence of two modes of star formation: 'normal' galaxies which lie in a well-defined parameter space (the 'main sequence') defined in a plot of sSFR versus redshift, and 'starburst' galaxies which present an excess in sSFR related to an increment of efficiency in compact star-forming regions probably triggered by the merger of two or more galaxies (e.g. Daddi et al. 2010). The controversy comes from the fact that these results are sensitive to the way by which

[1] *Herschel* is an ESA space observatory with science instruments provided by the European-led Principal Investigator consortia and with important participation from NASA.

Table 1. Broad-band data used in this work. Noise (rms) values are obtained from the pixel fluctuation seen in the whole area used for stacking, including the normalization η found between fitted peaks and catalogued fluxes (see Section 3.1.5). Note that these values are slightly different with respect to published ones. The references for each of the catalogues and images are as follows: UDS: 24 μm, from the *Spitzer* UKIDSS UDS [SpUDS; data version delivery S18.7 from the NASA/IPAC Infrared Science Archive (http://irsa.ipac.caltech.edu/data/SPITZER/docs/spitzermission/observingprograms)]; 70 μm, from the *Spitzer* Wide-area Infrared Extragalactic Survey (Surace et al. 2005, data version delivery DR3-S11 retrieved from the NASA/IPAC Infrared Science Archive); *Herschel* PACS 100- and 160-μm data from the HerMES survey [UDS deep level-3 field; reduced as in Ibar et al. (2010) but using an improved cosmic ray removal]; SPIRE 250-, 350- and 500-μm maps (SMAP_v4.2; Levenson et al. 2010) and catalogues (SCAT_SXT_iDR1; Smith et al. 2012) retrieved from the *Herschel* Database in Marseille (HeDaM; http://hedam.oamp.fr/HerMES/index.php) of the HerMES survey; AzTEC 1100-μm data taken at JCMT (Austermann et al. 2010). COSMOS: 24 and 70 μm, from the *Spitzer* coverage of the COSMOS field [S-COSMOS; GO2+GO3a+GO3b Delivery v1 from the NASA/IPAC Infrared Science Archive (http://irsa.ipac.caltech.edu/Missions/spitzer.html); Sanders et al. 2007; Le Floc'h et al. 2009; Frayer et al. 2009]; PACS 100 and 160 μm from the PEP survey; SPIRE 250, 350 and 500 μm from HerMES (SMAP_v4.2 and SCAT_SXT_iDR1 from HeDaM); AzTEC 1100-μm data taken at ASTE (Scott et al. 2008).

Telescope/ detector	Central λ (μm)	FWHM (arcsec)	Pixel size (arcsec)	rms [UDS] (mJy beam^{-1})	rms [COSMOS] (mJy beam^{-1})
Spitzer-MIPS	24	6.0	1.2	0.025	0.022
Spitzer-MIPS	70	18.2	4.0	3.7	2.8
Herschel-PACS	100	7.03	2.0	2.1	1.9
Herschel-PACS	160	11.55	3.0	4.7	4.3
Herschel-SPIRE	250	18.15	6.0	5.5	4.5
Herschel-SPIRE	350	25.15	8.33	6.3	5.3
Herschel-SPIRE	500	36.30	12.0	7.1	5.8
JCMT-AzTEC	1100	18.0	3.0	1.4	
ASTE-AzTEC	1100	30.0	3.0		1.4

'star-forming galaxies' are selected (Karim et al. 2011; Sobral et al. 2011) as the sSFR can change as more passive galaxies satisfy the applied selection criteria (Cirasuolo et al., in preparation).

To explore the intimate relationship between SFR, M_* and $A_{\rm H\alpha}$, we make use of ∼2 deg^2 image by the High-redshift Emission Line Survey[2] (HiZELS; Geach et al. 2008; Sobral et al. 2009, 2013) in the Cosmic Evolution Survey (COSMOS; ∼1.45 square degree; Scoville 2007) and the United Kingdom Infrared Telescope (UKIRT) Infrared Deep Sky Survey (UKIDSS; Lawrence et al. 2007) Ultra Deep Survey (UDS, ∼ 0.67 square degree; Almaini et al., in preparation) fields. We extract a large and unique sample of relatively low-luminosity [$L(\rm H\alpha)_{obs} \approx 10^{41.7-42.7}$ erg s^{-1}] star-forming galaxies, using a tuned narrow-band-filter technique to pick up large numbers of simultaneous Hα and [O II] (if available) emitters (alleviating the need for spectroscopic redshifts) at a well-defined $z = 1.47$ redshift (Sobral et al. 2012).

Taking advantage of the plethora of multiwavelength coverage in the UDS and COSMOS fields, we describe the far-IR (rest-frame 8–1000-μm) properties of the HiZELS sample using data taken by *Spitzer* Multiband Imaging Photometer (MIPS; Rieke et al. 2004) at 24 and 70 μm; *Herschel* Photodetector Array Camera and Spectrometer (PACS; Poglitsch et al. 2010) at 100 and 160 μm as part of the PACS Evolutionary Probe (PEP; Lutz et al. 2011) survey; *Herschel* Spectral and Photometric Imaging Receiver (SPIRE; Griffin et al. 2010) at 250, 350 and 500 μm as part of the *Herschel* Multitiered Extragalactic Survey (HerMES[3]; Oliver et al. 2012); and the Astronomical Thermal Emission Camera (AzTEC; Wilson et al. 2008) at 1100 μm while mounted at the James Clerk Maxwell Telescope (JCMT) and at the Atacama Submillimeter Telescope Experiment (ASTE) – more details about these data are given in Table 1. Similar works were done for a sample at $z = 2.23$ by Geach et al. (2008) using *Spitzer* at 70 and 160 μm, achieving upper limits near the peak of the Spectral Energy Distribution (SED), and at $z = 0.84$ using 24-μm imaging (Garn et al. 2010).

Direct Hα measurements, in combination with *Spitzer*, *Herschel* and AzTEC imaging provide an ideal framework for a detailed description of the star formation activity at $z = 1.47$ (near the peak of cosmic star formation history, where most of the galaxy mass was assembled; e.g. Dickinson et al. 2003), and its dependences on parameters such as luminosity, stellar mass, [O II]/Hα ratio and rest-frame colours. We mainly make use of a recent parametrization of the SFR (Kennicutt et al. 2009) based on a linear combination of the observed Hα and bolometric far-IR (rest-frame 8–1000-μm) luminosities. This estimate is suitable for both far-IR- and optically selected star-forming galaxies.

In this paper, the sample is described in Section 2 and our analysis of the stacked far-IR measurements is explained in Section 3. The results are discussed in Section 4 and our conclusions are summarized in Section 5. Throughout the text, we adopt a Salpeter IMF (Salpeter 1955) and estimate the contribution from the thermally pulsing asymptotic giant branch (TP-AGB; e.g. Trujillo et al. 2007) in our derived stellar masses. We use a Λ cold dark matter cosmology with $H_0 = 70$ km s^{-1} Mpc^{-1}, $\Omega_{\rm M} = 0.3$ and $\Omega_\Lambda = 0.7$.

2 THE SAMPLE OF Hα EMITTERS AT $z = 1.47$

HiZELS uses narrow-band filters to detect Hα emission at a variety of redshifts, up to $z = 2.23$ (Sobral et al. 2013). Given the nature of the Hα emission, HiZELS selects only young star-forming galaxies and AGN. Distinguishing between Hα and any other emission lines at other redshift is a critical step. Double-matched narrow-band

[2] For more details on the survey, progress and data release, see http://www.roe.ac.uk/ifa/HiZELS

[3] http://hermes.sussex.ac.uk

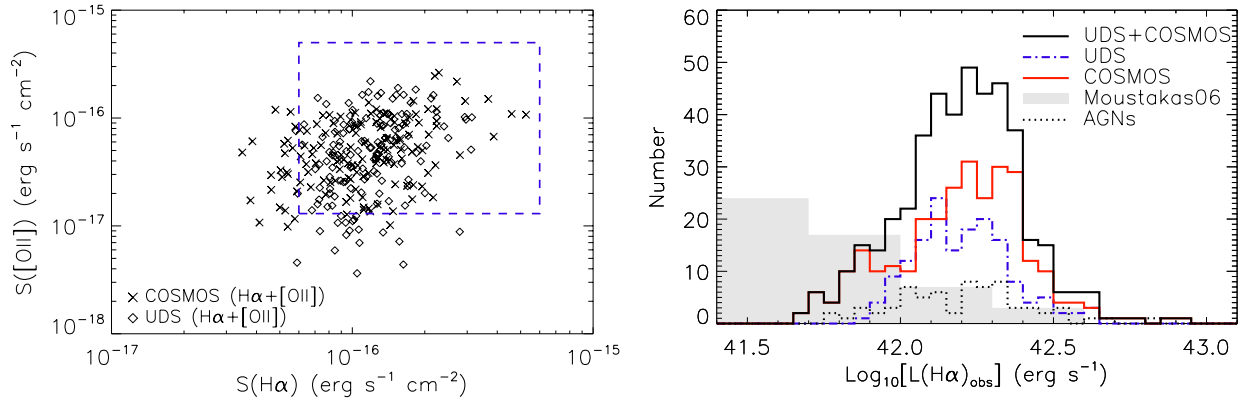

Figure 1. Left: measured narrow-band Hα and [O II] fluxes for sources in the UDS and COSMOS fields. The dashed rectangle shows the region used to show the consistency of stacked signals from both fields (see Fig. 2, left). Right: distribution of observed Hα luminosities (corrected for [N II] contamination but not for extinction). The black (thick solid), blue (dot–dashed) and red (solid) lines: the merged, UDS and COSMOS samples, respectively. The black dotted line shows the identified AGN distribution as described in Section 2.1. The shaded area corresponds to the bright end of the source distribution used to calibrate the Kennicutt et al. (2009) SFR correlations in the local Universe (Moustakas et al. 2006).

surveys detecting strong emission lines offer a good way of mitigating this problem (e.g. Sobral et al. 2012). For star-forming galaxies at $z \sim 1.5$ we make use of the fact that the Hα line is detectable in the *H* band while the [O II]-372.7-nm emission can be observed at the red end of the z' band. As shown in Sobral et al. (2012), by combining deep broad-band photometry with tuned double-narrow-band imaging – where the NB921 narrow-band filter on *Subaru*/Suprime-Cam detects [O II] and the NB_H filter on UKIRT/Wide Field Camera detects Hα at the same redshift – it is possible to conduct an effective survey of line-emitting sources at $z = 1.47$.

We extract HiZELS samples from Sobral et al. (2012, 2013) which provide uniform Hα coverage across the UDS, reaching an average effective flux limit (3σ) of $S_{H\alpha} \approx 9 \times 10^{-17}$ erg s^{-1} cm^{-2}, while the matched *Subaru* ([O II]) narrow-band survey reaches an effective flux of $S_{[O\,II]} \approx 9 \times 10^{-18}$ erg s^{-1} cm^{-2}. The depth of the NB921 imaging provides counterparts for all Hα emitters in the UDS and therefore allows a clean selection of the Hα sample. In COSMOS, the Hα narrow-band imaging was intentionally designed to obtain a 'wedding cake' survey (i.e. deeper than UDS in small regions), while the [O II] imaging has relatively uniform coverage, resulting in a large number of COSMOS Hα emitters without an [O II] detection (∼50 per cent). For a cleaner selection of Hα emitters and no other emission line objects, we make use of the available broad-band photometry in these fields. As described in Sobral et al. (2012), we use colour–colour criteria (a method similar to the *BzK* diagnostic; Daddi et al. 2004) in a $B - R$ versus $i - K$ diagram to first remove low-redshift contaminants, and then in $i - z$ versus $z - K$ to remove the high-redshift emitters (e.g. [O III] and Hβ). From all Hα candidates, these colour–colour criteria and the matched [O II] detection remove ∼ 50 per cent of the candidates, resulting in a tight redshift distribution ($\Delta z \approx 0.02$) as evidenced by the small number of sources with available spectroscopic redshifts (∼5 per cent of the sample). The total number of Hα emitters identified by HiZELS at $z = 1.47 \pm 0.02$ is 188 in UDS and 325 in COSMOS fields.

Sobral et al. (2013) estimate that after applying the mentioned colour–colour criteria to a sample which does not present NB921–[O II] detections, the level of contamination of emitting galaxies at different redshifts is of the order of ∼ 15 per cent. Some of these contaminants could come from Hβ, [O III] or [O II] at $z = 2.2$ and 3.3, or possibly from galaxies at $z < 1$ over a wide range of possible emission lines. Given that ∼50 per cent of COSMOS galaxies lack [O II] detections due to no data being available, or because it is too shallow, we expect that the overall contamination in the COSMOS sample should be of the order of ∼7.5 per cent, i.e. ∼5 per cent in the full UDS+COSMOS sample. We do not expect these contaminants to distribute in well-defined redshifts, so their contribution to the stacks is unknown. We assume that a possible contamination of 5 per cent will not be sufficient to significantly modify the median stacks of our analysis.

In Fig. 1 we show the observed Hα luminosity distribution [$L(H\alpha)_{obs}$, not corrected for extinction] for the HiZELS samples. Values of $L(H\alpha)_{obs}$ have been corrected by removing the flux estimated to be contributed by the adjacent [N II] doublet at 654.8 and 658.3 nm, following Villar et al. (2008), as presented in Sobral et al. (2012). Based on a recent estimation of the point spread function (PSF) in the narrow-band images, the Hα and [O II] photometry increases by ∼30 per cent with respect to those presented in Sobral et al. (2012, 2013). This is an aperture correction factor introduced to take into account the flux missed at >2 arcsec radius. The observed luminosity distribution can be roughly characterized by $L(H\alpha)_{obs} = 10^{42.2 \pm 0.2}$ erg s^{-1}, i.e. to an equivalent $SFR_{H\alpha} \approx 32$ M$_\odot$ yr^{-1} (Kennicutt 1998), assuming an average extinction of 1 mag for the Hα luminosities. We note that these observed luminosities are within the range of those which define the SFR correlations in the local Universe (see Fig. 1; Kennicutt et al. 2009, using sources from Moustakas, Kennicutt & Tremonti 2006), although we are inevitably biased against extreme extinction (undetected at Hα; $A_{H\alpha} \gtrsim 3$) and towards galaxies with high SFR and young stellar populations.

2.1 Removing AGN from the sample

We have deliberately chosen a conservative approach to account for AGN contamination. We have removed all sources previously catalogued at X-ray wavelengths (Ueda et al. 2008; Cappelluti et al. 2009) as this ∼2 keV emission at $z = 1.47$ is expected to be produced via inverse Compton scattering by a compact and highly ionized region surrounding an AGN. We might remove some sources presenting powerful thermal X-ray emission, although this should not affect our analysis as only six and three sources are X-ray emitters in the UDS and COSMOS fields, respectively. We have also used available 1.4-GHz images (Schinnerer et al. 2010; Arumugam et al., in preparation) to identify synchrotron emission produced by an AGN. Assuming a typical $SFR_{H\alpha} \approx 32$ M$_\odot$ yr^{-1} for the

HiZELS population (based on $A_{H\alpha} = 1$) and the validity of the far-IR/radio correlation at high redshift (Ibar et al. 2008; Ivison et al. 2010a), we remove all sources having 1.4-GHz flux densities larger than 150 μJy given that their expected radio luminosities would put them $>4\sigma$ away from the far-IR/radio correlation. In addition, similar to Garn et al. (2010) we use template SEDs of star-forming galaxies and AGN to fit the multiwavelength broad-band photometry available for our sources (see Section 3.6). All those best fitted as AGN are identified with red rest-frame mid-IR colours. We average the observed *Spitzer*-3.6- and 4.5-μm fluxes to estimate the rest-frame 1.6-μm flux density, and the 5.8- and 8.0-μm fluxes for the 2.8-μm rest-frame flux density. All SED-fitted AGN, the bulk of the X-ray sources and those sources spectroscopically classified as AGN using the Baldwin, Phillips and Terlevich diagram (Stott et al. 2013, Sobral et al., in preparation) are identified to have a rest-frame flux density ratio 2.8 μm/1.6 μm > 1. We apply this simple threshold to remove further potential AGN from the sample. Note that this near-IR criterion is the same that makes Lacy et al. (2004) and Stern et al. (2005) methods work, but we optimize it for $z = 1.47$ galaxies in order to minimize the errors in the *Spitzer* Infrared Array Camera (IRAC) photometry.

These criteria (X-ray/radio/mid-IR) identify a total of 30 (6/9/22) and 40 (3/5/35) potential AGN in the UDS and COSMOS fields, respectively. Some of them are identified by more than one criterion. Our final star-forming galaxy sample consist of 443 sources (158 in UDS and 285 in COSMOS) at a well-defined redshift, $z = 1.47$.

3 THE FAR-IR PROPERTIES OF HIZELS GALAXIES

We describe the far-IR properties of the HiZELS sample by taking advantage of the plethora of multiwavelength coverage in the UDS and COSMOS fields. We note, however, that out of 443 selected star-forming galaxies, only 10 (2 per cent) of them have catalogued *Herschel*/SPIRE-250-μm sources (Smith et al. 2012) within 2 arcsec – the most sensitive band near the peak of the far-IR SED. They all have $S_{250\,\mu m} < 40$ mJy at a significance of $\lesssim 5\sigma$ and there is no particular trend for 250-μm fluxes with observed Hα luminosity. In contrast, within the possible AGN population there are five detections (out of 70, i.e. 7 per cent) at 250 μm suggesting typically brighter far-IR luminosities for this population. These small number of detections, however, are not sufficient to provide a robust view to the HiZELS population as a whole.

In this paper, we use a stacking analysis to tackle the far-IR properties of the Hα galaxies. Stacking is a statistical method which consists of cutting out a significant number of map regions centred at the position of known sources (e.g. see details at Kurczynski & Gawiser 2010; Béthermin et al. 2012b; Heinis et al. 2013). When all these maps are averaged together (pixel by pixel), signals at the image's centre can emerge from the noise. These signals represent averaged (or median) properties for the stacked population. The reliability of this approach highly depends on the common nature of the parent population, where statistical quantities are robust.

3.1 Stacking and flux density measurements

In this work, all images we use for stacking (at 24, 70, 100, 160, 250, 350, 500 and 1100 μm) have resolutions (full width at half-maximum, FWHM) much larger than the subarcsec astrometric uncertainties of the HiZELS sample (∼0.25 arcsec), so for simplicity we confidently assume that the resulting stacked signals are 'point like'. Images do not cover exactly the same sky area (see Table 1), so these differences imply that sources outside the coverage, or in noisy regions, are flagged differently for each map. The percentages of stacked sources per image are shown in Table 2.

Table 2. The percentage of HiZELS galaxies (from a total of 158 in UDS and 285 in COSMOS) presenting imaging coverage at different wavelengths. Almost all images provide more than 90 per cent coverage, with the exemption of both AzTEC images which miss ∼20 per cent of the sources, and the deep *Herschel*-PACS UDS map which only covers 40 per cent of the sample (see PACS errors in Fig. 2).

λ (μm)	UDS Cov (per cent)	COSMOS Cov (per cent)
24	94	100
70	100	100
100	39	97
160	39	97
250	100	100
350	100	100
500	100	100
1100	79	78

We use arbitrary 91 pixel × 91 pixel × N (where N is the number of stacked sources) data cubes for each waveband. Maps extracted from the images (S_i) are centred at the closest map pixel to the source position. The data cubes are then collapsed by taking the median signal in each map pixel yielding simple 91 × 91-pixel^2 images for each waveband. We prefer a median stack as this minimizes the effect produced by outliers (e.g. by nearby bright galaxies) in the map-pixel distributions. In most cases, especially at 24, 250 and 350 μm, a clear signal appears at the image centre (results are shown in Table 4).

In each of the stacked maps, we remove the median sky background level (B_{MC}). This level is estimated using a Monte Carlo simulation (100 realizations following the same approach to create the stacks) randomizing the source positions within 5 arcmin from their original locations. This background subtraction is found to be essential in order to properly co-add stacked signals coming from different fields (see equation 1).

3.1.1 *Spitzer stacks*

In *Spitzer* images (see Table 1), we use a 2D-Gaussian fit (IDL routine MPFIT2PEAK; Markwardt et al. 2009) to extract the central stacked peaks. The fit is performed using the following constraints: the peak must be close to the central position (ΔRA, ΔDec. < FWHM/2); the sky level is fixed at zero (since the background has already been subtracted); the width (FWHM) is fixed at the appropriate one for a point source (as given in Table 1). From these Gaussian fits we extract the peak value. Note that *Spitzer* images are in units of MJy sr^{-1}, so this peak value needs a conversion factor to obtain the integrated flux density (see Section 3.1.5). In particular, we have arbitrarily increased (by three times) the uncertainty of the 24-μm data point, to account for the highly varied mid-IR spectra of star-forming galaxies at $z = 1.47$.

3.1.2 *Herschel-PACS stacks*

For *Herschel*-PACS images from PEP and HerMES surveys, we extract fluxes using aperture photometry with a radius of 10 and 15 arcsec at 100 and 160 μm, respectively. Aperture photometry is preferred in PACS mainly due to the uncertainties on the peak

of the PSF (introduced by the telemetry of the *Herschel* telescope and by the asymmetry seen along the scan directions). We have divided the COSMOS-PEP images by factors of 1.151 and 1.174 at 100 and 160 μm, respectively, in order to match the calibration products used to create the UDS-HerMES image (a change from responsivity FM,5 to FM,6 within the *Herschel* Interactive Processing Environment). This translates into an aperture correction of the order of 30 per cent at those aperture radii. PACS images are in units of Jy pixel^{-1}, so we simply use the IDL routine APER to integrate fluxes, not performing background subtraction as this has been already removed.

3.1.3 Herschel-SPIRE stacks

Following the same recipe used to extract stacked *Spitzer* fluxes, we measure integrated flux densities by simply measuring the peak in the Gaussian fits. This is valid given that *Herschel*-SPIRE HerMES images (at 250, 350 and 500 μm) are in Jy beam^{-1} units and we are assuming 'point-like' stacks. Details about these images can be found in Levenson et al. (2010).

3.1.4 AzTEC stacks

Given that AzTEC images come from different telescopes, the co-addition of these stacked images needs to include a Gaussian convolution of the JCMT image (FWHM 18 arcsec; Austermann et al. 2010) to match the ASTE resolution (30 arcsec; Scott et al. 2008). Similar to *Herschel*-SPIRE, these maps are in Jy beam^{-1} units, so integrated flux densities are measured by the peak of a Gaussian fit (same constraints as those used for *Spitzer* stacks).

3.1.5 Empirical calibration

To account for possible biases introduced by the way we measure stacked flux densities, we use the released catalogues from each image to find the median and scatter (3σ clipped) of the ratio between catalogued flux densities (between 5 and 10σ) and fitted Gaussian peaks (aperture photometry for the PACS case). We call this ratio $\eta = S_{\rm FIT}/S_{\rm CAT}$. We note that for *Herschel* and AzTEC images, η is within 15 per cent from unity, although for *Spitzer* images η is the value to convert ster-radians to beams. We apply these normalization factors to the extracted flux densities in order to make the calibration of each stacked data point dependent on the released catalogues from each of the different images (see Table 1). In the cases when we merge the UDS and COSMOS fields, we use the average correction found between both fields (usually within 10 per cent of each other).

In summary, for a given number of UDS ($N_{\rm UDS}$) and COSMOS ($N_{\rm COSMOS}$) sources, the calibrated flux density measured from their co-added stacked signals can be expressed as

$$\mathrm{MED}(S) = \eta \times \mathrm{MED}\left[\left(S_{i=1,\ldots,N_{\rm UDS}} - B_{\rm MC,UDS}\right) \cup \left(S_{j=1,\ldots,N_{\rm COSMOS}} - B_{\rm MC,COSMOS}\right)\right],$$

where MED stands for the median over all the cut-out map signals S_i, $B_{\rm MC}$ corresponds to the Monte Carlo simulated sky background obtained by randomizing the positions around the source sample for each field, and ∪ stands for the co-addition of signals coming from different fields. We find that the detection significance (fitted peak over local pixel rms) of each stacked data point ranges at $<15\sigma$, where the 24-, 250- and 350-μm bands provide the clearest detections.

Errors in our measurements are estimated using the same Monte Carlo simulations (100 realizations) to obtain the averaged pixel rms noise for *Spitzer*, *Herschel*-SPIRE and AzTEC stacks, and the averaged uncertainty using random aperture photometry on *Herschel*-PACS stacks. We assume a conservative 10 per cent absolute calibration uncertainty (added in quadrature) for all IR bands (e.g. Stansberry et al. 2006; Austermann et al. 2010; Swinyard et al. 2010). Finally for consistency, we normalize our estimated uncertainties using the η ratio.

3.1.6 Clustering effects

The clustering of galaxies can induce a bias on stacking measurements (Béthermin et al. 2010, 2012b; Kurczynski & Gawiser 2010; Heinis et al. 2013). Béthermin et al. (2012b) estimated that for 24-μm-selected samples, the level of clustering could increase the stacked peak flux measurements in the order of 7, 10 and 20 per cent at 250, 350 and 500 μm, respectively. This effect is larger in lower resolution images and it is seen as wings around the stacked signals. These wings reflect the effect produced by the excess of probability to find sources around another one. Béthermin et al. (2012b) showed that the shape of this wing is the autocorrelation function ($\omega(\theta) = A_{\rm CF}\theta^{\beta_{\rm CF}}_{\rm CF}$) convolved by the PSF. The amplitude of this signal thus depends on the mean flux of the clustered population and the amplitude of clustering. A preliminary view to the angular correlation function of HiZELS galaxies at $z = 1.47$ ($\sim$150–300 sources deg^{-2}) shows it is well behaved with a power law ($\beta_{\rm CF} = -0.8$ and $A_{\rm CF} \approx$ 10–20 with no clear evidence for a steeper correlation function at smaller scales) suggesting that these galaxies reside in relatively typical dark matter haloes of $\sim 10^{11}$–$10^{12}\,{\rm M}_{\odot}$ (see e.g. Sobral et al. 2010; Geach et al. 2012) – similar (or slightly lower) to the ones expected to host 24-μm sources (Béthermin, Doré & Lagache 2012a; Wang et al. 2013).

In this work, we have neglected the effect of clustering due to three main reasons: (1) Béthermin et al. (2012b) estimated clustering effects using mean stacks while we use median ones. This implies that we considerably reduce the contribution of objects to clustering signal, while contribution of sources below the confusion limit stays the same; (2) Hα-selected galaxies have stellar masses which are typically lower than far-IR-selected ones (see Section 4.2), hence the effect of clustering is expected to be lower. Actually, we do not see any clear excess of 'wing' emission in our *Herschel* stacked images; (3) the effect that clustering has in stacked SPIRE flux densities using 24-μm-selected galaxies is roughly in the range of the global uncertainties in our work.

3.2 SED fitting

We parametrize the stacked SEDs using a modified blackbody (MBB) spectrum in the Rayleigh–Jeans regime, but truncated to a power law in the mid-IR (Wein side). The measured bolometric far-IR luminosities, $L(8-1000\,\mu{\rm m})$, are obtained by integrating the SED in rest-frame frequencies between $\nu_1 = 0.3$ THz (1000 μm) and $\nu_2 = 37.5$ THz (8 μm),

$$L(8-1000\,\mu{\rm m}) = 4\pi\, D_{\rm L}^2(z) \int_{\nu_1/(1+z)}^{\nu_2/(1+z)} S_\nu \,{\rm d}\nu, \quad (1)$$

where the flux density per unit frequency is parametrized as

$$S_\nu(\nu) = A \times \begin{cases} {\rm MBB}(\nu) & \text{if} \quad \nu \leq \nu_\star \\ {\rm MBB}(\nu_\star) \times \nu^{\alpha_{\rm mid-IR}} & \text{if} \quad \nu > \nu_\star \end{cases}$$

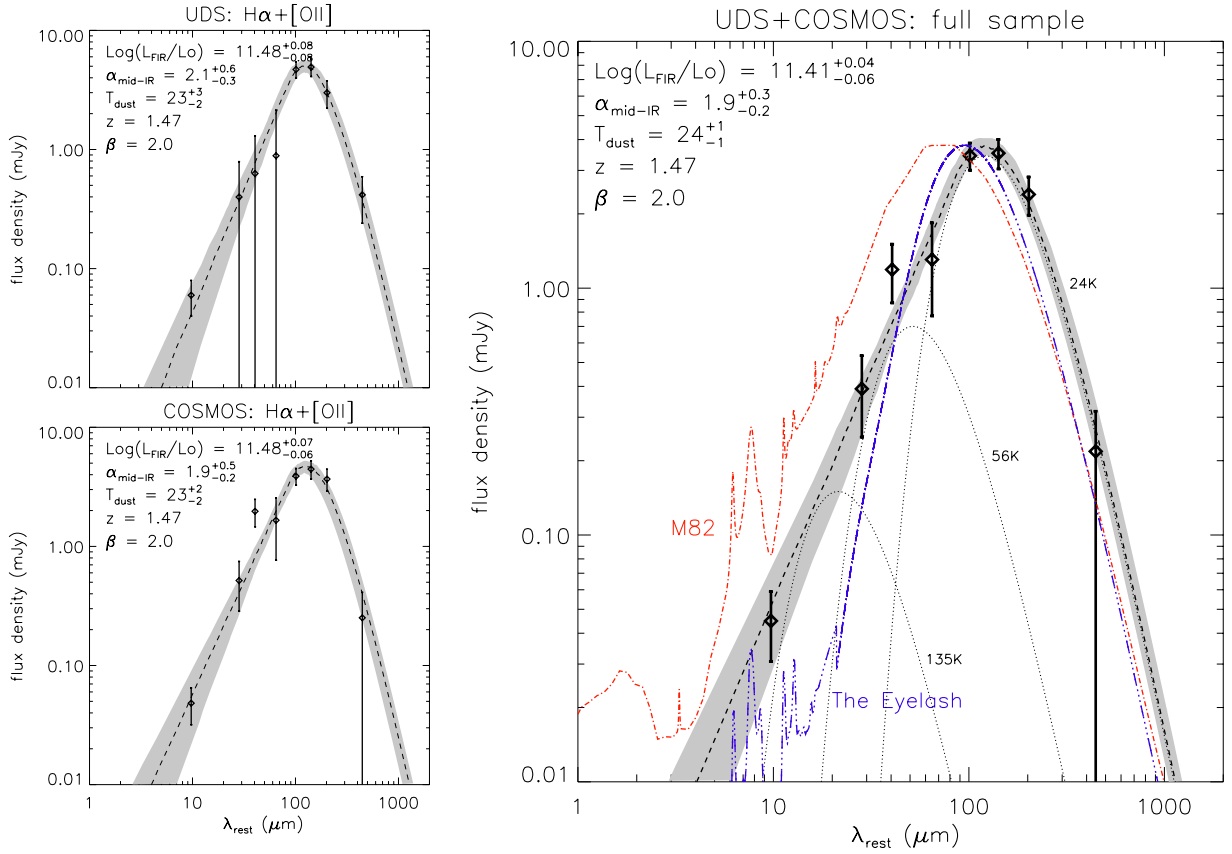

Figure 2. The stacked far-IR flux densities obtained for different HiZELS samples at $z = 1.47$. Photometry points come from *Spitzer* (24 and 70 μm), *Herschel* (100, 160, 250, 350 and 500 μm) and AzTEC (1100 μm) images (see Table 1 for references). The dashed lines show the expected median SED value based on Monte Carlo realizations repeating the SED fits by varying the photometry using the errors for each data point (see Section 3.1). Derived parameters are provided in the inset values (see also Table 5) while the plotted shaded areas represent the 68-per cent confidence levels. Left: the stacked far-IR SED for the HiZELS samples with detected $S(\mathrm{H}\alpha) > 6 \times 10^{-17}$ erg s^{-1} cm^{-2} and $S([\mathrm{O\,II}]) > 1.3 \times 10^{-17}$ erg s^{-1} cm^{-2} in the UDS (top) and COSMOS (bottom) panels. Right: the large panel shows the stacked SED for the full HiZELS sample, compared to two star-forming galaxies: M82 (a local starburst galaxy with an SED obtained from a fit to the observed photometry presented by Silva et al. 1998) and the Cosmic Eyelash (a gravitationally lensed galaxy at $z = 2.3$ – Ivison et al. 2010b), both normalized to arbitrary values. At wavelengths longward of 10 μm, the stacked SED can be approximated by the superposition of three MBB functions with temperatures of 135, 56 and 24 K (using $\beta = 2.0$), and luminosity contributions of 3.5, 16.3 and 80.2 per cent, respectively.

and

$$\mathrm{MBB}(\nu) = \frac{\nu^{3+\beta}}{\exp\left[\frac{h\,\nu}{k\,T_{\mathrm{dust}}}(1+z)\right] - 1}.$$

Here, β is the dust emissivity index (e.g. Seki & Yamamoto 1980; Dunne et al. 2011) modulating the Planck function to cover a wider range of dust temperatures (fixed to $\beta = 2$), and ν_* is obtained numerically at

$$\frac{\mathrm{d}\log_{10}(\mathrm{MBB})}{\mathrm{d}\log_{10}(\nu)}(\nu_\star) = \alpha_{\mathrm{mid-IR}}$$

to match the slope of the Planck function and the power law at ∼100–200 μm. Examples of SED fits applied to our stacked signals are shown in Fig. 2.

In our estimates, we assume the redshift is fixed at $z = 1.47$ [luminosity distance, $D_{\mathrm{L}}(z) = 10641$ Mpc], and parameters h and k refer to Planck and Boltzmann constants, respectively. To fit the observed stacks we have three free parameters in our model: A (the normalization of the fits), T_{dust} (as in the MBB function) and $\alpha_{\mathrm{mid-IR}}$ (the slope in the mid-IR). The best fit for each parameter is obtained by minimizing χ^2. All quoted errors correspond to the 68 per cent confidence levels obtained using an end-to-end Monte Carlo (100 realizations) fit to the SED using perturbed photometry based on the estimated errors of each stack (assuming Gaussianity).

3.2.1 *Robustness of the SED fit approach*

Our SED fits parametrize the mid-IR range assuming a simple spectral slope, which is not physically well motivated, but at least it does not bias the derived far-IR luminosities. We demonstrate this by using stacked signals coming from different parent HiZELS samples, then fitting them alternating between β and $\alpha_{\mathrm{mid-IR}}$ as fixed and free parameters. Comparing both outputs, we find that far-IR luminosities and dust temperatures are not biased by this assumption. The main reason we preferred to fix β, rather than $\alpha_{\mathrm{mid-IR}}$, is due to the low signal-to-noise ratio in the AzTEC 1100-μm stacks. This 1100-μm data point provides the main constraint on β, but it is usually only an upper limit. In our initial analysis we used $\beta = 1.5$, but we found that this produced SED fits which in several cases violated the AzTEC 1100-μm upper limits, and gave rise to dust temperatures ∼5 K (∼1σ) higher than those obtained when fixing $\alpha_{\mathrm{mid-IR}} = 2.0$ with β as a free parameter (see discussion of the T_{dust}–β relation by Shetty et al. 2009 and Smith et al., in preparation).

To test the robustness of our SED routine, we used a different fitting approach involving ∼7000 SED library models (Siebenmorgen & Krügel 2007) to reproduce the far-IR photometry via a χ^2 minimization (Symeonidis et al. 2009, 2011). We find that our derived far-IR luminosities are systematically 10 per cent lower with respect to this other method. This offset is, however, within the 1σ errors. The difference is mostly seen in the mid-IR part of the spectrum. The SED libraries include prominent polycyclic aromatic hydrocarbon (PAH) features and a systematic excess of warm dust emission at $\lambda_{\rm rest} \sim 20\,\mu$m, compared to our simple mid-IR power law. This demonstrates the uncertainties introduced by the SED fits and the actual capabilities for precisely measuring luminosities in this work. On the other hand, in terms of dust temperatures we find that our fits (using $\beta = 2$) and the library SED fits are in good agreement with no clear systematic.

3.3 The star formation rate and Hα extinction

Our study provides a unique opportunity to directly measure the typical SFR of the HiZELS sample. There is no unbiased SFR indicator and it is well documented that the use of inconsistent extinction corrections and SED assumptions are the primary source for the large scatter seen by different estimators (Wijesinghe et al. 2011), especially at high redshifts (e.g. Hopkins & Beacom 2006). As described in Section 2, a key advantage of our HiZELS sample is that it does not differ significantly from the intrinsic luminosities of the local star-forming galaxies used to calibrate the SFR indicators (see Fig. 1). Indeed, the conditions defined by Kennicutt et al. (2009) in section 6.2 of their paper are fully satisfied by the HiZELS sample. Hence, assuming no cosmic evolution of the parameters controlling the SFR (e.g. the IMF) and the absence of AGN contamination in the Hα luminosities, we can confidently assume that (Kennicutt 1998)

$$\mathrm{SFR}(\mathrm{M}_\odot\,\mathrm{yr}^{-1}) = 7.9\times10^{-42}\times L(\mathrm{H}\alpha)_{\rm int}\quad \mathrm{erg\,s}^{-1}, \tag{2}$$

where $L(\mathrm{H}\alpha)_{\rm int}$ is the intrinsic Hα luminosity (corrected for dust attenuation). This is the canonical definition for the SFR, assuming solar abundances and a simple power-law slope for the IMF, $\mathrm{d}N/\mathrm{d}m \propto m^{-2.35}$ (Salpeter 1955), integrated between 0.1 and 100 $\mathrm{M}_\odot$. A way to estimate the extinction for deriving $L(\mathrm{H}\alpha)_{\rm int}$ is by combining the measured Hα and far-IR luminosities as follows:

$$L(\mathrm{H}_\alpha)_{\rm int} = L(\mathrm{H}\alpha)_{\rm obs} + a_{\rm FIR}\times L(8{-}1000\,\mu\mathrm{m})\quad \mathrm{erg\,s}^{-1}, \tag{3}$$

i.e. the far-IR luminosity carries the information for the amount of dust extinction, where $a_{\rm FIR} = (2.5\pm0.6)\times10^{-3}$ (Kennicutt et al. 2009). Equation (3) can be understood as the balance of the contributions from unobscured and obscured emission to the total SFR in a galaxy, and $a_{\rm FIR}$ determines the ratio at which the components are comparable. The ratio between the two components can be used to trace the averaged extinction for the sample,

$$A_{\mathrm{H}\alpha}(\mathrm{mag}) = 2.5\times\log_{10}\left(1 + a_{\rm FIR}\frac{L(8{-}1000\,\mu\mathrm{m})}{L(\mathrm{H}\alpha)_{\rm obs}}\right) \tag{4}$$

a measure which is expected to be less sensitive to possible ageing effects given that attenuation decreases with increasing stellar age (Kennicutt et al. 2009). As a reference, the typical Hα extinction for optically selected star-forming galaxies in the local (e.g. Garn & Best 2010) and high-redshift (e.g. Garn et al. 2010; Sobral et al. 2012; Stott et al. 2013) Universe is $A_{\mathrm{H}\alpha} \approx 1$ mag.

Note that since our study uses stacked signals (median properties), we treat equations (2)–(4) in terms of probability distributions using Monte Carlo simulations, bootstrapping the error for the median value of the Hα distribution (Fig. 1) and the measured stacked far-IR flux errors.

3.4 The global far-IR properties of the star-forming HiZELS population

In the left-hand panel of Fig. 2, we compare the stacked far-IR fluxes of all those UDS and COSMOS HiZELS galaxies with narrow-band Hα and [O II] detections (see Fig. 1). Both samples produce consistent far-IR fluxes to within the uncertainties, suggesting that we can merge them to increase the overall sample size and to allow an alternative sample selection to investigate the far-IR properties as a function of different observed physical parameters. The stacked fluxes obtained from the merged full sample are shown in Fig. 2 and derived parameters presented in Tables 4 and 5.

The observed SEDs peak roughly at 280 μm (rest frame ∼113 μm) corresponding to a dust temperature, $T_{\rm dust} \sim 24$ K. As noted in Section 3.2.1, this value increases to ∼30 K when $\beta = 1.5$ is used. The assumption of a simple mid-IR power law is useful to mitigate the larger uncertainties at shorter wavelengths (especially on *Spitzer*-70-μm and PACS-100-/160-μm photometry), where we usually find $\alpha_{\rm mid-IR} = 2$, e.g. similar to that observed in M82. We find that the use of a MBB is essential to fit the stacked SED. This makes perfect sense since the stacked fluxes include the MBB emission from each independent galaxy as well as the broadening introduced by stacking Hα emitters with different dust temperatures (the expected $z = 1.47\pm0.02$ distribution has a negligible effect compared to these two effects). In our SED fits, this broadening is basically modulated by β and $\alpha_{\rm mid-IR}$. Alternatively, in Fig. 2 we show that the typical HiZELS SED (at $\lambda > 10\,\mu$m) can be approximated by the composition of three MBB functions with $T_{\rm dust} = 24$, 56 and 135 K (using $\beta = 2.0$), contributing in 80.2, 16.3 and 3.5 per cent to the total far-IR luminosity.

The derived median far-IR luminosity for the whole merged sample is $L(8{-}1000\,\mu\mathrm{m}) = 10^{11.41^{+0.04}_{-0.06}}\,\mathrm{L}_\odot$, i.e. our Hα emitters are typically luminous infrared galaxies (LIRGs) at $z = 1.47$. The ratio between the far-IR and the observed Hα luminosities is ∼1000:2, similar to the $a_{\rm FIR}$ factor from equation (3). This implies that these two components (unobscured and obscured) have comparable contributions to the total SFR. Using equation (4), we derive a median $A_{\mathrm{H}\alpha} = 1.0\pm0.2$ mag, in good agreement with typical values seen in local and high-z star-forming galaxies (Garn & Best 2010; Sobral et al. 2012; Stott et al. 2013).

Given that our sample has been primarily selected by its Hα power, we cannot assume HiZELS galaxies work as calorimeters (Lacki et al. 2010). Indeed, this is the main reason we prefer the use of a combination of Hα and far-IR luminosities to derive total SFRs (Kennicutt et al. 2009), rather than Hα or far-IR luminosities alone (Kennicutt 1998). In Table 3, we present the different methods used to compare SFR estimates in this work. For example, assuming a simple $A_{\mathrm{H}\alpha} = 1$ to get the intrinsic Hα luminosity, the $\mathrm{SFR}_{\mathrm{H}\alpha,\mathrm{A}_{\mathrm{H}\alpha}=1}$ is roughly within 1.4–3 times of that derived using $\mathrm{SFR}_{\rm FIR}$ or $\mathrm{SFR}_{24\,\mu\mathrm{m}}$ stacks. This simple comparison reinforces the fact that a non-negligible fraction of the starlight has escaped from these galaxies. We find that the $\mathrm{SFR}_{\rm FIR}$ are typically 1.5 times larger than those expected from $\mathrm{SFR}_{\mathrm{H}\alpha,\,\rm FIR}$ (Section 4.1). In particular, we note that the use of the 24-μm flux density as an SFR indicator at $z = 1.47$ is relatively uncertain compared to $\mathrm{SFR}_{\rm FIR}$. This is due to the combination of being estimated using a single photometry point and due to the large uncertainty induced by the Silicate absorption

Table 3. Different methods to measure the median SFR for the whole population of HiZELS galaxies at $z = 1.47$ (443 sources). Hα and far-IR luminosities are in erg s^{-1} while output values are in M$_\odot$ yr^{-1}. Our preferred SFR parametrization is in bold at the top of the list, SFR$_{\mathrm{H}\alpha,\,\mathrm{FIR}}$ (see Section 4.1; Kennicutt et al. 2009). The five equations (SFR$_{\mathrm{H}\alpha,\mathrm{A}_{\mathrm{H}\alpha}}$) refer to the canonical SFR definition (see equation 2) provided by Kennicutt (1998) using different parametrization for Hα extinction (scatter of ∼0.3 mag) – taken from Garn & Best (2010) and Sobral et al. (2012) (see bottom of table). Values for M_* are given in M$_\odot$ (note the 1.21 factor is to match our assumed Salpeter IMF and TP-AGB component, see Section 3.6) and rest-frame $u-z$ colour in Vega magnitudes. SFR$_{\mathrm{FIR}}$ is defined in Kennicutt (1998) and solely uses the far-IR luminosity to derive the rate of star formation. SFR$_{24\,\mu\mathrm{m}}$ is defined by Rieke et al. (2009) in which we have derived $A_{24} = 0.54$ and $B_{24} = 1.80$ by interpolating their table 1 at $z = 1.47$ (see equation 14 of their paper). Note that $4\pi \mathrm{D}_\mathrm{L}^2 \times \mathrm{S}_{24\,\mu\mathrm{m}}$ is in units of Jy cm^2, where D_L is the luminosity distance and $S_{24\,\mu\mathrm{m}}$ the flux density at 24 μm.

	Method	SFR (M$_\odot$ yr^{-1})
SFR$_{\mathrm{H}\alpha,\mathrm{FIR}}$	**$=7.9\times10^{-42}\times[L(\mathrm{H}\alpha)_{\mathrm{obs}}+a_{\mathrm{FIR}}\times L(8\text{–}1000\ \mu\mathrm{m})]$**	**$= 32 \pm 5$**
SFR$_{\mathrm{H}\alpha,\mathrm{A}_{\mathrm{H}\alpha}=0}$	$= 7.9 \times 10^{-42} \times L(\mathrm{H}\alpha)_{\mathrm{obs}}$	$=13.1 \pm 0.3$
SFR$_{\mathrm{H}\alpha,\mathrm{A}_{\mathrm{H}\alpha}=1}$	$= 7.9 \times 10^{-42} \times L(\mathrm{H}\alpha)_{\mathrm{obs}} \times 10^{0.4}$	$=31.9 \pm 0.8$
SFR$_{\mathrm{H}\alpha,\mathrm{A}_{\mathrm{H}\alpha}([\mathrm{O\,II}]/\mathrm{H}\alpha)}$	$= 7.9 \times 10^{-42} \times L(\mathrm{H}\alpha)_{\mathrm{obs}} \times 10^{0.4\,A_{\mathrm{H}\alpha}([\mathrm{O\,II}]/\mathrm{H}\alpha)}$	$=28.9 \pm 1.4$
SFR$_{\mathrm{H}\alpha,\mathrm{A}_{\mathrm{H}\alpha}(M_*)}$	$= 7.9 \times 10^{-42} \times L(\mathrm{H}\alpha)_{\mathrm{obs}} \times 10^{0.4\,A_{\mathrm{H}\alpha}(M_*)}$	$=24.8 \pm 0.7$
SFR$_{\mathrm{H}\alpha,\mathrm{A}_{\mathrm{H}\alpha}([u-z]_{\mathrm{rest}})}$	$= 7.9 \times 10^{-42} \times L(\mathrm{H}\alpha)_{\mathrm{obs}} \times 10^{0.4\,A_{\mathrm{H}\alpha}([u-z]_{\mathrm{rest}})}$	$=22.9 \pm 0.6$
SFR$_{\mathrm{FIR}}$	$= 4.5 \times 10^{-44} \times L(8\text{–}1000\ \mu\mathrm{m})$	$= 44^{+4}_{-6}$
SFR$_{24\,\mu\mathrm{m}}$	$= 10^{\mathrm{A}_{24}+\mathrm{B}_{24}\times[\log(4\pi \mathrm{D}_\mathrm{L}^2\times \mathrm{S}_{24\,\mu\mathrm{m}})-53]}$	$=90 \pm 18$
where		
$A_{\mathrm{H}\alpha}([\mathrm{O\,II}]/\mathrm{H}\alpha)$	$= -4.30\,X^4 - 11.30\,X^3 - 7.39\,X^2 - 2.94\,X + 0.31$	using $X = \log_{10}([\mathrm{O\,II}]/\mathrm{H}\alpha)$
$A_{\mathrm{H}\alpha}(M_*)$	$= -0.09\,X^3 + 0.11\,X^2 + 0.77\,X + 0.91$	using $X = \log_{10}(M_*/10^{10}/1.21)$
$A_{\mathrm{H}\alpha}([u-z]_{\mathrm{rest}})$	$= -0.092\,X^3 + 0.671\,X^2 - 0.952\,X + 0.875$	using $X = (u-z)_{\mathrm{rest}}$

band at 9.8 μm, PAH line emissions and possible AGN power-law components redshifted into the 24-μm band.

3.5 The AGN population

In Section 2.1, we explained the conservative method we have used to clean the HiZELS sample of possible AGN contamination. Note that this method might have classified some powerful star-forming galaxies as AGN. Using our X-ray/mid-IR/radio criteria we have identified a total of 70 possible AGN within our HiZELS sample.

Using the same stacking approach explained above, we show in Fig. 3 the typical far-IR SED for the HiZELS galaxies classified as AGN. We compare the full stacked star-forming sample (presented in Fig. 2, right) with respect to that of the AGN population, finding that the typical far-IR luminosities for AGN are slightly higher ($\sim 10^{11.56\,\pm\,0.08}$ L$_\odot$). There is evidence for warmer dust temperatures ($\Delta T_{\mathrm{dust}} \sim 7$ K) with respect to the star-forming galaxies. It is interesting to see that AGN do not dominate the mid-IR part of the stacked SEDs – even though we would expect some mid-IR emission coming from the central torus-like region surrounding the AGN, introducing an excess at 24 μm (9.7 μm, rest frame).

As a sanity check, we performed the same analysis, leaving the identified AGN in the sample. We find that there is no significant variation of the results presented in Figs 5 and 6, and all general tracks are maintained within a fraction of the 1σ errors.

We conclude that given the number of identified AGN is small with respect to the whole sample (∼15 per cent), possible biases introduced in median stacked signals are minimized unless AGN are the dominant population. There is no evidence suggesting such scenario.

3.6 Dependency of SFR on Hα luminosity and stellar mass

In Fig. 5, we explore far-IR-derived quantities in order to understand the mechanisms controlling the star formation activity of HiZELS at $z = 1.47$. We present how the far-IR luminosity $L(8-1000\ \mu\mathrm{m})$, the dust temperature, the derived SFR$_{\mathrm{H}\alpha,\,\mathrm{FIR}}$ (see Table 3) and the Hα extinction (equation 4) correlate with the observed (and intrinsic) Hα luminosity and stellar mass. We are able to create three bins for each parameter, with sufficiently large and similar number of sources in each bin to define the SED accurately. We find a relatively mild dependency for far-IR luminosity on observed L(Hα), and stellar mass, but a significant linear slope (at 5σ significance) on intrinsic L(Hα). The SED-fitting uncertainties hide any trends in dust temperature, T_{dust}, but values are in rough agreement with previous *Herschel*-selected samples which are assumed to be mostly

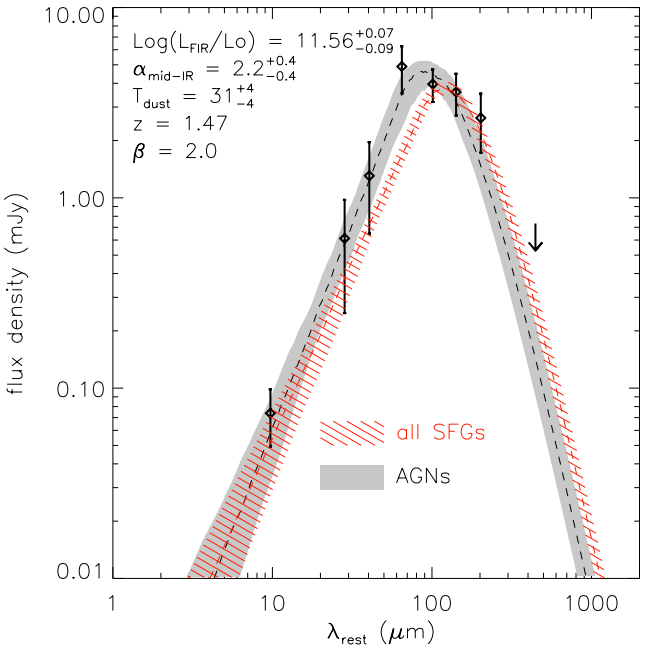

Figure 3. Stacked SED for all possible AGN (grey shaded region), including radio-loud, X-ray-detected and mid-IR identified ones (see Section 2.1 for details). The derived far-IR properties for the AGN sample are inset at the top-left. The stacked AGN SED is compared to the one obtained from all HiZELS star-forming galaxies (red line filled; presented in Fig. 2, right).

Table 4. The stacked far-IR fluxes found for the different selection criteria presented throughout this HiZELS study. 'Ref.' stands for a reference number (see Table 5). In the column 'Field': U = UDS and C = COSMOS. '*N*' corresponds to the total number of sources in the HiZELS sample satisfying the 'Selection criterion'. Details on the flux density measures and Monte Carlo-based errors are described in Section 3.1. Flux densities and errors are corrected by the empirical calibration factor η (see Section 3.1.5). If fluxes are zero, then the measured flux was found to be negative.

Ref.	Field	Selection criterion	N	$S_{24\,\mu m}$ (mJy)	$S_{70\,\mu m}$ (mJy)	$S_{100\,\mu m}$ (mJy)	$S_{160\,\mu m}$ (mJy)	$S_{250\,\mu m}$ (mJy)	$S_{350\,\mu m}$ (mJy)	$S_{500\,\mu m}$ (mJy)	$S_{1100\,\mu m}$ (mJy)
1	C	$S(\mathrm{H}\alpha) > 6 \times 10^{-17}$ and $S([\mathrm{O\,II}]) > 1.3 \times 10^{-17}$	113	0.05±0.02	0.52 ± 0.23	1.97 ± 0.51	1.66 ± 0.89	3.89 ± 0.62	4.46 ± 0.78	3.68 ± 0.77	0.25 ± 0.16
2	U	$S(\mathrm{H}\alpha) > 6 \times 10^{-17}$ and $S([\mathrm{O\,II}]) > 1.3 \times 10^{-17}$	123	0.06 ± 0.02	0.40 ± 0.39	0.63 ± 0.67	0.89 ± 1.25	4.70 ± 0.73	4.92 ± 0.82	3.00 ± 0.78	0.42 ± 0.18
3	U+C	all	443	0.04 ± 0.01	0.39 ± 0.14	1.19 ± 0.32	1.31 ± 0.53	3.44 ± 0.43	3.52 ± 0.48	2.40 ± 0.42	0.22 ± 0.10
4	U+C	$41.6 < \log_{10}[L(\mathrm{H}\alpha)_{\mathrm{obs}}] \leq 42.1$	129	0.04 ± 0.01	0.46 ± 0.24	1.31 ± 0.43	0.88 ± 1.03	3.20 ± 0.59	3.85 ± 0.74	2.26 ± 0.72	0.22 ± 0.16
5	U+C	$42.1 < \log_{10}[L(\mathrm{H}\alpha)_{\mathrm{obs}}] \leq 42.25$	133	0.05 ± 0.02	0.31 ± 0.26	1.64 ± 0.57	1.27 ± 0.97	4.12 ± 0.63	4.18 ± 0.73	2.95 ± 0.69	0.26 ± 0.17
6	U+C	$42.25 < \log_{10}[L(\mathrm{H}\alpha)_{\mathrm{obs}}] \leq 43.0$	181	0.05 ± 0.02	0.47 ± 0.23	1.15 ± 0.40	2.17 ± 0.84	3.17 ± 0.51	2.76 ± 0.57	2.01 ± 0.57	0.22 ± 0.17
7	U+C	$41.6 < \log_{10}[L(\mathrm{H}\alpha)_{\mathrm{int}}([\mathrm{O\,II}]/\mathrm{H}\alpha)] \leq 42.4$	85	0.04 ± 0.02	0.26 ± 0.32	1.23 ± 0.58	0.00 ± 1.24	2.90 ± 0.69	3.31 ± 0.85	2.33 ± 0.89	0.27 ± 0.20
8	U+C	$42.4 < \log_{10}[L(\mathrm{H}\alpha)_{\mathrm{int}}([\mathrm{O\,II}]/\mathrm{H}\alpha)] \leq 42.6$	69	0.04 ± 0.02	0.43 ± 0.39	1.28 ± 0.73	0.00 ± 1.52	5.17 ± 0.86	6.11 ± 1.05	4.25 ± 1.00	0.33 ± 0.24
9	U+C	$42.6 < \log_{10}[L(\mathrm{H}\alpha)_{\mathrm{int}}([\mathrm{O\,II}]/\mathrm{H}\alpha)] \leq 44.1$	121	0.07 ± 0.02	0.54 ± 0.30	1.98 ± 0.56	3.31 ± 1.02	4.23 ± 0.66	4.17 ± 0.75	2.95 ± 0.73	0.07 ± 0.18
10	U+C	$41.6 < \log_{10}[L(\mathrm{H}\alpha)_{\mathrm{int}}(M_*)] \leq 42.4$	151	0.02 ± 0.01	0.04 ± 0.23	0.85 ± 0.33	0.00 ± 1.08	1.38 ± 0.48	1.68 ± 0.59	0.92 ± 0.61	0.08 ± 0.15
11	U+C	$42.4 < \log_{10}[L(\mathrm{H}\alpha)_{\mathrm{int}}(M_*)] \leq 42.6$	127	0.04 ± 0.01	0.29 ± 0.27	0.35 ± 0.46	0.66 ± 0.98	2.85 ± 0.57	2.73 ± 0.67	1.98 ± 0.68	0.29 ± 0.19
12	U+C	$42.6 < \log_{10}[L(\mathrm{H}\alpha)_{\mathrm{int}}(M_*)] \leq 44.1$	162	0.10 ± 0.03	0.91 ± 0.24	1.99 ± 0.43	2.89 ± 0.79	6.16 ± 0.75	6.20 ± 0.81	4.47 ± 0.71	0.40 ± 0.17
13	U+C	$41.6 < \log_{10}[L(\mathrm{H}\alpha)_{\mathrm{int}}([u-z]_{\mathrm{rest}})] \leq 42.4$	153	0.04 ± 0.01	0.33 ± 0.23	1.14 ± 0.41	0.00 ± 0.88	2.54 ± 0.52	2.98 ± 0.64	1.79 ± 0.65	0.14 ± 0.15
14	U+C	$42.4 < \log_{10}[L(\mathrm{H}\alpha)_{\mathrm{int}}([u-z]_{\mathrm{rest}})] \leq 42.6$	172	0.04 ± 0.01	0.41 ± 0.23	0.93 ± 0.42	1.74 ± 0.75	3.60 ± 0.55	3.53 ± 0.62	2.48 ± 0.60	0.22 ± 0.16
15	U+C	$42.6 < \log_{10}[L(\mathrm{H}\alpha)_{\mathrm{int}}([u-z]_{\mathrm{rest}})] \leq 44.1$	115	0.08 ± 0.02	0.54 ± 0.27	1.58 ± 0.48	2.33 ± 0.92	4.36 ± 0.66	4.41 ± 0.77	3.36 ± 0.74	0.41 ± 0.21
16	U+C	$9.5 < \log_{10}[\mathrm{M}_*/\mathrm{M}_\odot] \leq 9.9$	90	0.03 ± 0.01	0.22 ± 0.30	0.30 ± 0.57	0.01 ± 1.16	2.04 ± 0.62	1.74 ± 0.75	1.02 ± 0.78	0.00 ± 0.21
17	U+C	$9.9 < \log_{10}[\mathrm{M}_*/\mathrm{M}_\odot] \leq 10.3$	443	0.06 ± 0.02	0.66 ± 0.27	1.52 ± 0.47	1.43 ± 0.87	4.37 ± 0.59	4.37 ± 0.65	2.60 ± 0.58	0.21 ± 0.15
18	U+C	$10.3 < \log_{10}[\mathrm{M}_*/\mathrm{M}_\odot] \leq 11.8$	443	0.07 ± 0.02	0.62 ± 0.22	1.68 ± 0.41	2.39 ± 0.73	5.20 ± 0.63	5.73 ± 0.72	3.91 ± 0.61	0.43 ± 0.14
19	U+C	$-1.20 < \log_{10}[[\mathrm{O\,II}]/\mathrm{H}\alpha] \leq -0.50$	84	0.05 ± 0.02	0.42 ± 0.36	2.09 ± 0.67	2.16 ± 1.16	3.45 ± 0.70	3.27 ± 0.82	2.28 ± 0.83	0.02 ± 0.22
20	U+C	$-0.50 < \log_{10}[[\mathrm{O\,II}]/\mathrm{H}\alpha] \leq -0.25$	90	0.07 ± 0.02	0.42 ± 0.31	1.81 ± 0.59	1.04 ± 1.23	5.78 ± 0.82	5.51 ± 0.91	3.62 ± 0.85	0.38 ± 0.20
21	U+C	$-0.25 < \log_{10}[[\mathrm{O\,II}]/\mathrm{H}\alpha] \leq 0.40$	101	0.04 ± 0.01	0.37 ± 0.31	1.43 ± 0.55	0.20 ± 0.97	3.27 ± 0.67	3.51 ± 0.80	2.81 ± 0.83	0.22 ± 0.19
22	U+C	$-0.5 < (u-z)_{\mathrm{rest}} \leq 0.9$	146	0.02 ± 0.01	0.25 ± 0.26	0.11 ± 0.45	0.00 ± 0.91	1.32 ± 0.47	1.32 ± 0.58	1.06 ± 0.61	0.33 ± 0.18
23	U+C	$0.9 < (u-z)_{\mathrm{rest}} \leq 1.5$	153	0.05 ± 0.02	0.43 ± 0.23	1.30 ± 0.46	1.98 ± 0.85	3.01 ± 0.54	2.86 ± 0.63	1.59 ± 0.61	0.00 ± 0.16
24	U+C	$1.5 < (u-z)_{\mathrm{rest}} \leq 3.0$	139	0.10 ± 0.03	0.71 ± 0.25	2.19 ± 0.51	2.47 ± 0.89	6.87 ± 0.83	7.28 ± 0.93	5.09 ± 0.80	0.44 ± 0.17
25	U+C	$19.0 < 3.6\,\mu\mathrm{m} \leq 21.1$	117	0.12 ± 0.04	0.91 ± 0.29	1.93 ± 0.58	3.82 ± 1.00	8.47 ± 0.99	8.76 ± 1.08	5.84 ± 0.90	0.46 ± 0.19
26	U+C	$21.1 < 3.6\,\mu\mathrm{m} \leq 22.1$	142	0.05 ± 0.02	0.35 ± 0.24	1.47 ± 0.48	1.62 ± 0.92	3.28 ± 0.57	3.17 ± 0.66	1.87 ± 0.63	0.20 ± 0.17
27	U+C	$22.1 < 3.6\,\mu\mathrm{m} \leq 25.0$	136	0.01 ± 0.01	0.00 ± 0.24	0.03 ± 0.43	0.00 ± 0.79	0.00 ± 0.46	0.40 ± 0.58	0.59 ± 0.62	0.00 ± 0.17
28	U+C	AGN	70	0.07 ± 0.02	0.61 ± 0.36	1.31 ± 0.66	4.90 ± 1.36	3.96 ± 0.77	3.60 ± 0.89	2.63 ± 0.90	0.00 ± 0.24

Table 5. The derived far-IR properties found for the different selection criteria ('Ref.' are same as in Table 4) presented throughout this HiZELS study. The median and the 68 per cent distribution of the observed Hα luminosity is presented in the second column. The fitting procedure used to extract the far-IR properties is explained in Section 3.2.

Ref.	$\log_{10}[L(\mathrm{H}\alpha)_{\mathrm{obs}}]$ (68 per cent distribution)	$\log_{10}[L(8-1000\,\mu\mathrm{m})/\mathrm{L}_{\odot}]$	$\mathrm{SFR}_{\mathrm{H}\alpha,\mathrm{FIR}}$ ($\mathrm{M}_{\odot}\,\mathrm{yr}^{-1}$)	$A_{\mathrm{H}\alpha}$ (mag)	T_{dust} (K)	$\alpha_{\mathrm{mid-IR}}$
1	$42.23^{+0.18}_{-0.19}$	$11.48^{+0.07}_{-0.06}$	$36.2^{+6.9}_{-6.3}$	$1.1^{+0.2}_{-0.2}$	23^{+2}_{-2}	$1.9^{+0.5}_{-0.2}$
2	$42.22^{+0.13}_{-0.17}$	$11.48^{+0.08}_{-0.08}$	$36.2^{+7.3}_{-6.5}$	$1.1^{+0.2}_{-0.2}$	23^{+3}_{-2}	$2.1^{+0.6}_{-0.3}$
3	$42.22^{+0.15}_{-0.22}$	$11.41^{+0.04}_{-0.06}$	$32.1^{+5.4}_{-5.0}$	$1.0^{+0.2}_{-0.2}$	24^{+1}_{-1}	$1.9^{+0.3}_{-0.2}$
4	$41.99^{+0.08}_{-0.15}$	$11.39^{+0.07}_{-0.10}$	$25.9^{+5.8}_{-5.1}$	$1.3^{+0.2}_{-0.2}$	24^{+2}_{-2}	$2.0^{+0.4}_{-0.3}$
5	$42.18^{+0.06}_{-0.05}$	$11.45^{+0.06}_{-0.07}$	$33.2^{+6.6}_{-5.8}$	$1.1^{+0.2}_{-0.2}$	24^{+3}_{-2}	$2.1^{+0.4}_{-0.4}$
6	$42.35^{+0.13}_{-0.07}$	$11.39^{+0.06}_{-0.07}$	$36.2^{+5.8}_{-5.2}$	$0.8^{+0.2}_{-0.2}$	28^{+3}_{-3}	$2.0^{+0.4}_{-0.2}$
7	$42.02^{+0.13}_{-0.16}$	$11.36^{+0.07}_{-0.14}$	$24.8^{+5.9}_{-5.1}$	$1.2^{+0.2}_{-0.3}$	24^{+6}_{-3}	$2.0^{+0.6}_{-0.4}$
8	$42.18^{+0.10}_{-0.12}$	$11.53^{+0.06}_{-0.08}$	$37.7^{+7.9}_{-7.0}$	$1.2^{+0.2}_{-0.2}$	23^{+2}_{-2}	$2.3^{+0.4}_{-0.3}$
9	$42.30^{+0.16}_{-0.16}$	$11.55^{+0.06}_{-0.07}$	$42.3^{+7.8}_{-7.1}$	$1.1^{+0.2}_{-0.2}$	27^{+3}_{-3}	$2.0^{+0.3}_{-0.3}$
10	$42.05^{+0.12}_{-0.19}$	$11.12^{+0.13}_{-0.14}$	$18.7^{+4.9}_{-3.4}$	$0.8^{+0.3}_{-0.2}$	29^{+8}_{-8}	$2.0^{+0.6}_{-0.5}$
11	$42.26^{+0.08}_{-0.14}$	$11.25^{+0.10}_{-0.09}$	$27.9^{+5.0}_{-3.9}$	$0.7^{+0.2}_{-0.2}$	24^{+4}_{-3}	$2.2^{+0.4}_{-0.3}$
12	$42.34^{+0.14}_{-0.16}$	$11.69^{+0.04}_{-0.05}$	$53.9^{+10.0}_{-9.3}$	$1.2^{+0.2}_{-0.2}$	24^{+1}_{-1}	$1.7^{+0.3}_{-0.2}$
13	$42.04^{+0.09}_{-0.17}$	$11.31^{+0.10}_{-0.07}$	$24.4^{+5.3}_{-4.6}$	$1.1^{+0.2}_{-0.2}$	26^{+6}_{-4}	$2.0^{+0.4}_{-0.4}$
14	$42.24^{+0.08}_{-0.09}$	$11.40^{+0.06}_{-0.07}$	$32.9^{+5.6}_{-5.0}$	$0.9^{+0.2}_{-0.2}$	25^{+3}_{-2}	$2.0^{+0.4}_{-0.2}$
15	$42.38^{+0.15}_{-0.13}$	$11.54^{+0.05}_{-0.08}$	$44.9^{+7.7}_{-7.0}$	$0.9^{+0.2}_{-0.2}$	24^{+2}_{-1}	$1.8^{+0.3}_{-0.3}$
16	$42.23^{+0.12}_{-0.25}$	$11.18^{+0.16}_{-0.15}$	$25.1^{+6.2}_{-4.0}$	$0.6^{+0.2}_{-0.2}$	28^{+9}_{-8}	$2.2^{+0.5}_{-0.6}$
17	$42.22^{+0.15}_{-0.22}$	$11.51^{+0.04}_{-0.05}$	$37.4^{+6.9}_{-6.3}$	$1.1^{+0.2}_{-0.2}$	26^{+1}_{-2}	$1.9^{+0.4}_{-0.2}$
18	$42.22^{+0.15}_{-0.22}$	$11.59^{+0.04}_{-0.06}$	$42.6^{+8.1}_{-7.6}$	$1.3^{+0.2}_{-0.2}$	23^{+1}_{-1}	$1.8^{+0.2}_{-0.2}$
19	$42.18^{+0.22}_{-0.14}$	$11.46^{+0.07}_{-0.08}$	$33.8^{+7.1}_{-6.3}$	$1.1^{+0.2}_{-0.2}$	28^{+4}_{-4}	$2.0^{+0.6}_{-0.3}$
20	$42.21^{+0.15}_{-0.21}$	$11.59^{+0.07}_{-0.06}$	$42.6^{+8.8}_{-7.9}$	$1.3^{+0.2}_{-0.2}$	25^{+4}_{-1}	$2.2^{+0.4}_{-0.4}$
21	$42.14^{+0.17}_{-0.22}$	$11.39^{+0.09}_{-0.07}$	$29.7^{+6.3}_{-5.3}$	$1.1^{+0.2}_{-0.2}$	25^{+4}_{-4}	$2.0^{+0.5}_{-0.3}$
22	$42.23^{+0.16}_{-0.23}$	$10.98^{+0.16}_{-0.13}$	$20.8^{+3.6}_{-2.5}$	$0.5^{+0.2}_{-0.1}$	22^{+11}_{-4}	$2.0^{+0.6}_{-0.4}$
23	$42.22^{+0.16}_{-0.21}$	$11.40^{+0.07}_{-0.10}$	$32.0^{+6.0}_{-5.4}$	$1.0^{+0.2}_{-0.2}$	29^{+4}_{-4}	$2.0^{+0.6}_{-0.3}$
24	$42.19^{+0.15}_{-0.17}$	$11.70^{+0.04}_{-0.07}$	$49.9^{+10.4}_{-9.8}$	$1.5^{+0.2}_{-0.2}$	23^{+1}_{-1}	$1.8^{+0.3}_{-0.2}$
25	$42.20^{+0.16}_{-0.17}$	$11.77^{+0.04}_{-0.05}$	$56.9^{+12.2}_{-11.3}$	$1.6^{+0.2}_{-0.2}$	23^{+1}_{-1}	$1.8^{+0.3}_{-0.2}$
26	$42.22^{+0.15}_{-0.23}$	$11.41^{+0.07}_{-0.08}$	$32.4^{+5.9}_{-5.4}$	$1.0^{+0.2}_{-0.2}$	26^{+3}_{-2}	$2.0^{+0.6}_{-0.3}$
27	$42.20^{+0.15}_{-0.25}$	$10.64^{+0.24}_{-0.30}$	$16.3^{+3.0}_{-1.9}$	$0.2^{+0.2}_{-0.1}$	27^{+13}_{-11}	$1.8^{+0.7}_{-0.5}$
28	$42.22^{+0.21}_{-0.22}$	$11.56^{+0.07}_{-0.09}$	$40.2^{+8.8}_{-7.5}$	$1.2^{+0.2}_{-0.2}$	31^{+4}_{-4}	$2.2^{+0.4}_{-0.4}$

dominated by obscured star formation (e.g. Amblard et al. 2010; Hwang et al. 2010). $\mathrm{SFR}_{\mathrm{H}\alpha,\,\mathrm{FIR}}$ increases as a function of all three parameters, with $L(\mathrm{H}\alpha)_{\mathrm{int}}$ showing the strongest dependence (a 4.5σ significance in linear slope). We find an anticorrelation between Hα extinction and Hα luminosity, expected given the form of equation (4). Extinction increases at large stellar masses in agreement with the trend seen by Garn & Best (2010) (see Fig. 5 bottom-right panel). As with T_{dust}, we do not find any strong correlation for $\alpha_{\mathrm{mid-IR}}$. All the stacked fluxes and derived parameters are presented in Tables 4 and 5.

3.6.1 *Stellar masses*

Stellar masses are derived via SED-fitting routines using the method described by Sobral et al. (2011), making use of the UV to *Spitzer*-IRAC near-IR photometry available in the COSMOS and UDS fields (see Fig. 4). We have included the TP-AGB contribution (Bruzual 2007 templates) as it has a significant effect for young stellar populations at $z \approx 1.5$, compared to masses derived with previous Bruzual & Charlot (2003) SED libraries ($\sim$1.5 times lower values). To be consistent, the previously published HiZELS stellar masses (Sobral et al. 2011) are divided by a factor of 0.55 to change from a Chabrier (2003) IMF to a Salpeter IMF. Based on the sensitivity of the broad-band photometry, we find that we are unable to confidently constrain stellar masses lower than $10^{9.5}\,\mathrm{M}_{\odot}$, which defines our lower mass limit for this particular analysis. By excluding sources with $M_{*} < 10^{9.5}\,\mathrm{M}_{\odot}$ and poor χ^2 fits to the optical/near-IR SEDs, we remove $\sim$25 per cent of the full sample. Note that this cut in the sample is only performed to explore correlations as a function of stellar mass, not in the other analyses. The low stellar mass population tend to be biased towards the highest star formation efficiencies (see Fig. 8) – a population which might not be the most representative one.

The distribution of intrinsic Hα luminosities (using $A_{\mathrm{H}\alpha}([u-z]_{\mathrm{rest}})$; see different parametrizations in Table 3) versus stellar masses can be seen in Fig. 4. We see a large scatter between these two parameters (a Pearson's product moment correlation of 0.23 giving a 5 per cent probability of correlation), probably due to the relatively narrow range of luminosities and the large uncertainties associated with the Hα extinction corrections ($\Delta A_{\mathrm{H}\alpha} \approx 0.3$ mag in scatter; Sobral et al. 2012).

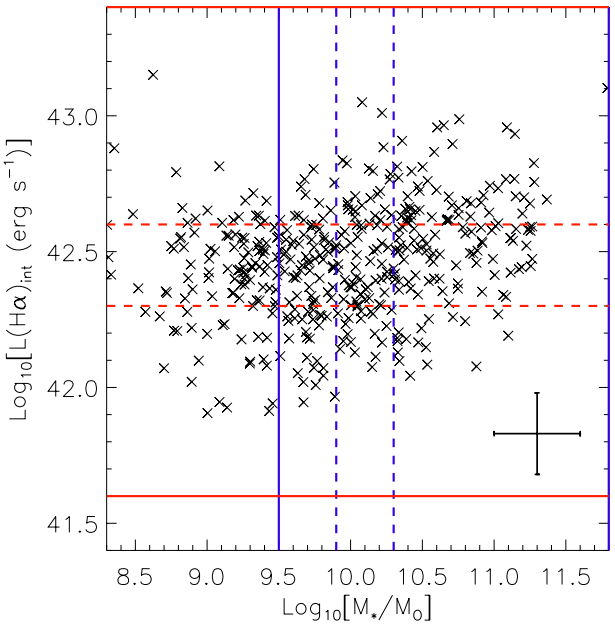

Figure 4. The distribution of intrinsic Hα luminosities versus SED-fitted stellar masses (see Section 3.6). $L(\mathrm{H}\alpha)_{\mathrm{int}}$ are obtained using the recipe provided by Sobral et al. (2012) which parametrize $A_{\mathrm{H}\alpha}$ as a function of the observed rest-frame $u-z$ colour (see Table 3). The typical error is shown at the bottom right of the figure. The solid blue/red lines define the minimum/maximum reliable range used for stacking. The dashed blue/red lines define the bins presented in Fig. 5.

3.7 Exploring other dependences

Given the difficulty of detecting Hβ at high-z (e.g. Stott et al. 2013), various parametrizations were created by Sobral et al. (2012) – based on SDSS data – to describe the Hα extinction at $z \sim 1.5$. In this section, we explore the parametrization of $A_{\mathrm{H}\alpha}$ as a function of the [O II]/Hα ratio, rest-frame $u-z$ colour and observed 3.6-μm magnitudes (see Fig. 6). By looking at the significance of the linear fit's slopes shown in Fig. 6, we find that the far-IR luminosity is not traced by the [O II]/Hα ratio, but depends strongly on intrinsic rest-frame $(u-z)$ colour and observed 3.6-μm photometry (rest frame $\sim K$ band).

[O II] is a collisionally excited doublet (λλ372.6, 372.9 nm) used as an SFR tracer for intermediate-redshift star-forming galaxies (e.g. Hayashi et al. 2013). It is sensitive to the abundance and the ionization state of the gas, and its luminosity is less directly coupled to the radiation fields from H II regions than Hα. Empirical evidence has shown a typical observed ratio of $L([\mathrm{O\,II}])/L(\mathrm{H}\alpha) = 0.23$ in massive galaxies (Hopkins et al. 2003). Sobral et al. (2012) proposed that this ratio could be used to parametrize the Balmer decrement (i.e. as a tracer of extinction), as they found that both parameters correlate after removing metallicity dependencies in a carefully selected SDSS galaxy sample. In Fig. 6, we show that this ratio does not have any clear correlation with our far-IR-derived parameters. This result might be explained by the fact that the $A_{\mathrm{H}\alpha}([\mathrm{O\,II}]/\mathrm{H}\alpha)$ parametrization induces a significantly broader extinction-corrected $\log_{10}[L(\mathrm{H}\alpha)_{\mathrm{int}}]$ histogram distribution (shown in the middle panels of Fig. 5). We suggest that this optical line ratio is a poor tracer of the far-IR luminosity and/or Hα extinction, but only sensitive to a relatively small number of unobscured star-forming regions, missing a significant fraction of the obscured star-forming clouds.

We have also looked at the correlation between $A_{\mathrm{H}\alpha}$ and galaxy colour (e.g. Sobral et al. 2012), finding a relatively strong dependence in rest-frame $(u-z)_{\mathrm{rest}}$ colour (linear slope at 4σ significance). This correlation suggests that red colours in a sample of young star-forming galaxies (Hα detected) are evidence of systems suffering large extinctions. We find that our trend agrees with Sobral et al.'s previous $A_{\mathrm{H}\alpha}([u-z]_{\mathrm{rest}})$ parametrization, although we see a higher level of extinction in redder colours. This suggests the appearance of a heavily obscured component not accounted by the previous optical measurements but revealed in the far-IR.

Finally, we explored how the far-IR luminosity depends on observed *Spitzer*-3.6-μm magnitudes. The observed 3.6 μm corresponds roughly to the rest-frame K band at $z = 1.47$, hence a proxy for the stellar mass of the galaxy. The K band versus $A_{\mathrm{H}\alpha}$ correlation is found to be slightly stronger than on stellar mass, suggesting this *Spitzer* band traces the old stellar populations but also some of the recent 'young' star-forming population.

4 DISCUSSION

4.1 SFR indicators

In this work, it is of major importance to use the best SFR estimator available in the literature. We note that HiZELS galaxies were selected by their Hα emission (in the rest-frame R band), so by definition considerable starlight must have escaped from these star-forming galaxies. This implies that HiZELS galaxies do not work as calorimeters (Lacki et al. 2010). Indeed, we have shown that $\mathrm{SFR}_{\mathrm{H}\alpha,\mathrm{A}_{\mathrm{H}\alpha}=0}$ (the Hα-derived SFR not corrected by extinction) is roughly within a factor of 3 to 4 to the far-IR-derived SFRs, clearly pointing out the importance of using a combination of Hα and far-IR measurements to obtain the total SFR (see also Iglesias-Páramo et al. 2006; Wijesinghe et al. 2011).

We find that our sample has a typical $L(\mathrm{H}\alpha)_{\mathrm{obs}}/L(8-1000\,\mu\mathrm{m}) \approx 2/1000$ ratio (similar to $a_{\mathrm{FIR}} = 2.5 \times 10^{-3}$, see equation 3). Considering also the fact that HiZELS Hα luminosities are similar (although at $z = 1.47$) to those used by Kennicutt et al. (2009) to determine the local SFR calibrations, we propose that the combination of Hα and far-IR luminosities ($\mathrm{SFR}_{\mathrm{H}\alpha,\,\mathrm{FIR}}$; Kennicutt et al. 2009) provides the most reliable SFR estimate for our particular study.

The HiZELS population at $z = 1.47$ is composed in its majority of LIRGs with $\mathrm{SFR}_{\mathrm{H}\alpha,\,\mathrm{FIR}} = 32 \pm 5\,\mathrm{M}_{\odot}\,\mathrm{yr}^{-1}$. They present typical Hα extinctions ($A_{\mathrm{H}\alpha} = 1.0 \pm 0.2$ mag) which are similar to those seen in local star-forming galaxies (i.e. in galaxies with lower SFRs). These results demonstrate the little evolution of the global Hα extinction properties previously seen by Sobral et al. (2012) and Stott et al. (2013) in HiZELS galaxies at $z = 1.47$.

4.1.1 An alternative SFR estimator

In the case when $L(\mathrm{H}\alpha)_{\mathrm{obs}} \ll a_{\mathrm{FIR}}\,L(8-1000\,\mu\mathrm{m})$ (see equation 3), the far-IR represents the dominant contribution to the SFR. In the literature, the transition from a dominant unobscured to a dominant obscured SFR component has usually been presented as a function of far-IR luminosity, using Hα (e.g. Villar et al. 2011), far-IR (e.g. Roseboom et al. 2012) or ultraviolet (e.g. Buat et al. 2010) samples. These correlations present large scatter but they all agree that the brighter the far-IR, the more dominant it becomes as a tracer of SFR.

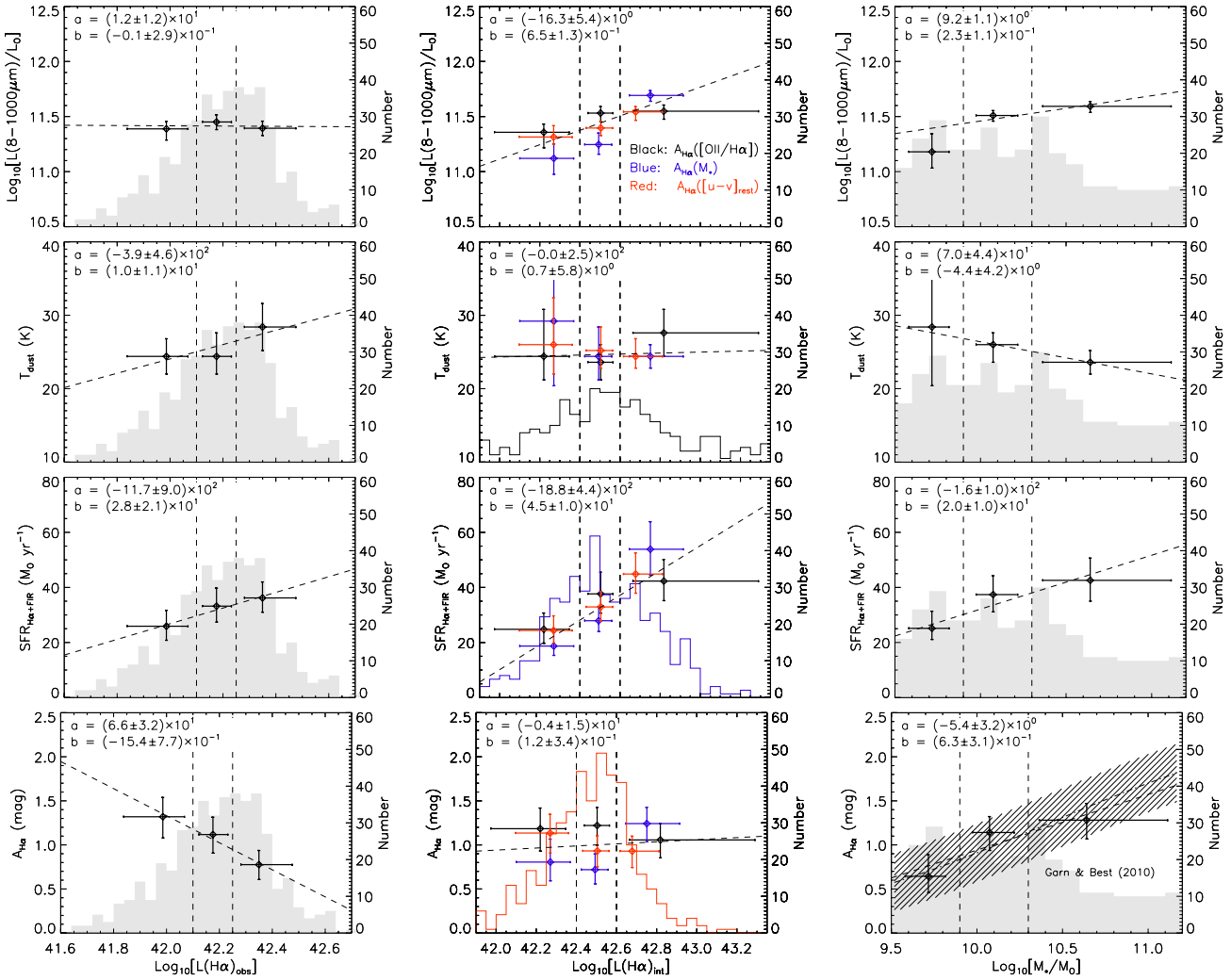

Figure 5. Plots showing (from top to bottom) the bolometric far-IR emission (8–1000 μm), the fitted dust temperature, the $\mathrm{SFR}_{\mathrm{H}\alpha,\,\mathrm{FIR}}$ (see Table 3) and the measured Hα extinction using equation (4) as a function of (from left to right) observed L(Hα), intrinsic L(Hα) (using the recipes provided in Table 3) and stellar mass (see Section 3.6). The histograms show the parameter distribution for the stacked population divided in three bins as defined by the vertical dashed lines. The coloured histograms in the middle panels show the $L(\mathrm{H}\alpha)_{\mathrm{int}}$ distributions using three different extinction corrections (following the same colours as the legend in the top-middle panel). The bottom-right panel includes the $A_{\mathrm{H}\alpha}(M_*)$ parametrization described in Garn & Best (2010) (see Table 3). Derived quantities and errors (1σ enclosing 68 per cent) are based on an end-to-end Monte Carlo realization of the fitting SED routine using the uncertainties measured in each of the stacked signals (Section 3.2), including the uncertainty in a_{FIR} from equation (3). These data points are presented in Table 5. The dotted lines show simple linear fits to the derived data points, $y(x) = a + b \times x$, where best-fitting parameters are inset at the top left of each figure and errors are 1σ uncertainty estimates for the returned parameters (obtained using LINFIT routine in IDL).

Making use of the dependences shown in Figs 5 and 6, we provide an empirical SFR estimate which can be used to alleviate the lack of far-IR measurements. We portray this idea in Fig. 7, where we show the ratio $\Phi = L(\mathrm{H}\alpha)_{\mathrm{obs}}/[L(\mathrm{H}\alpha)_{\mathrm{obs}} + a_{\mathrm{FIR}}\, L(8{-}1000\,\mu\mathrm{m})]$ as a function of three different parameters. Note that Φ ranges from 0 to 1 and traces the ratio between unobscured (observed Hα) and total (far-IR & Hα) SFR. We see that the observed Hα luminosity dominates (>50 per cent) the total SFR when galaxies have low stellar masses ($\lesssim 10^{9.8}$ $\mathrm{M}_{\odot}$), or blue colours ($[u-z]_{\mathrm{rest}} \lesssim 0.9$), or *Spitzer*-3.6-μm photometry fainter than 22 mag (Vega). For HiZELS at $z = 1.47$ (or similar population), we parametrize the SFR as follows:

$$\mathrm{SFR}_{\mathrm{H}\alpha,\Phi} = 7.9 \times 10^{-42}\, \frac{L(\mathrm{H}\alpha)_{\mathrm{obs}}}{\Phi}, \qquad (5)$$

where Φ is obtained empirically by a linear fit,

$$\log_{10}[\Phi] = A + B \times X. \qquad (6)$$

Note that Φ should be lower than unity and preferentially higher than 0.15 (see Fig. 7). We find $A = 0.03 \pm 0.16$ and $B = -0.35 \pm 0.15$ if X is the rest-frame $(u - z)$ colour or $A = -5.5 \pm 1.6$ and $B = 0.236 \pm 0.071$ if X is the observed *Spitzer*-3.6-μm magnitude. The bottom figure shows a weaker correlation as a function of stellar masses, although it indicates that sources with measured M_* have, in general, an SFR dominated by the far-IR emission.

As noted before, these empirical relations can be used to provide a better proxy for the SFR when far-IR estimates are absent for high-z Hα-emitting galaxies. This is especially useful for galaxies presenting high stellar masses, given that the far-IR luminosity

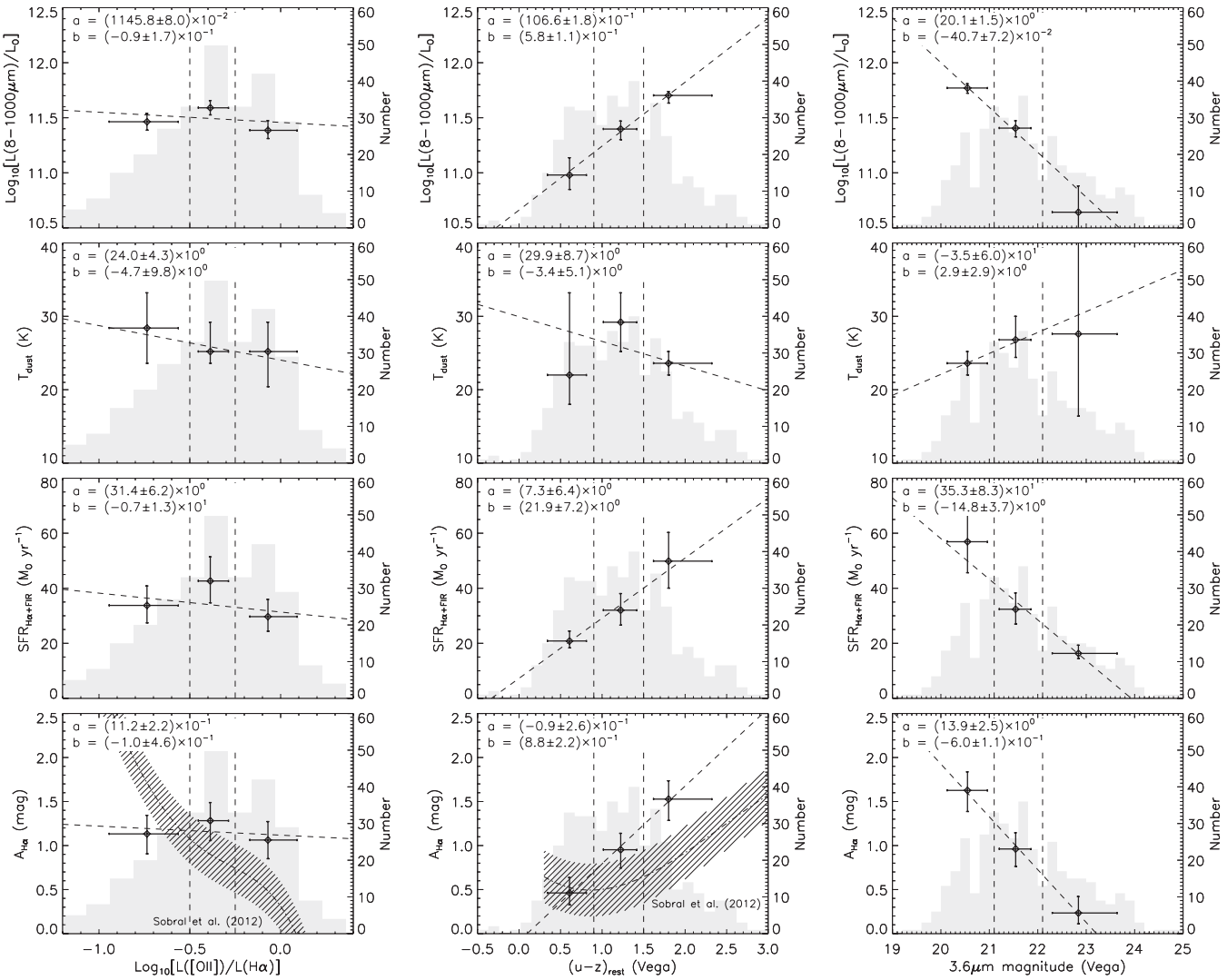

Figure 6. As Fig. 5, but this time showing the derived properties as a function of the $\log_{10}[L([\mathrm{O\,II}])/L(\mathrm{H}\alpha)]$ luminosity ratio, rest-frame $[u-z]_{\mathrm{rest}}$ colour and observed *Spitzer*-3.6-μm photometry. In the bottom figures, we compare our results with the $A_{\mathrm{H}\alpha}$ parametrizations presented by Sobral et al. (2012). We conclude that $L([\mathrm{O\,II}])/L(\mathrm{H}\alpha)$ does not correlate with the Hα extinction (defined in equation 3) as predicted by Sobral et al. (2012) using Balmer decrements. Significant correlations are found in terms of the simple observables, $(u-z)_{\mathrm{rest}}$ and 3.6 μm, which can be used to parametrize the obscured star formation in these Hα emitters (see equation 6). In particular, the bottom-middle panel suggests the appearance of a highly extinguished component in red galaxies which is not totally evidenced by optical studies (e.g. Sobral et al. 2012).

dominates over the observed Hα as a tracer of the SFR. We remind that these equations are only valid for the range of parameters discussed in this work, so extrapolations should be taken with caution.

4.1.2 A discrepancy in previous SFR tracers

We note that in the case when the far-IR emission is by far the dominant SFR tracer, the parametrizations from the literature ($\mathrm{SFR_{FIR}}$ and $\mathrm{SFR_{H\alpha,\,FIR}}$, see Table 3) do not agree. Indeed, the following ratio does not converge to unity when $L(\mathrm{H}\alpha)_{\mathrm{obs}} \rightarrow 0$:

$$\frac{\mathrm{SFR_{H\alpha,FIR}}}{\mathrm{SFR_{FIR}}} = \frac{7.9\times10^{-42}[L(\mathrm{H}\alpha)_{\mathrm{obs}} + 2.5\times10^{-3}L(8{-}1000\,\mu\mathrm{m})]}{4.5\times10^{-44}L(8{-}1000\,\mu\mathrm{m})}$$

$$= 0.44.$$

This is not related to the assumed IMF, as both estimates use Salpeter. The 0.44 factor tells us that, if the $\mathrm{SFR_{H\alpha,\,FIR}}$ calibration is correct, then the equation for the far-IR-only calibration assumes that there is a typical additional contribution of 2.27 times more star formation associated with an unobscured component not traced by the far-IR. The accuracy of this assumption will clearly depend on the nature of the population being studied. To recalibrate the SFR estimators is beyond the scope of this paper, although we stress the need to use the most suitable SFR tracer, based on the similarity to the parent population used to define the correlations in the local Universe.

4.2 Stellar masses and the far-IR power

Garn & Best (2010), using SDSS sources at $\langle z\rangle \approx 0.08$, showed that low-mass star-forming galaxies tend to have less extinction (less obscured star formation activity) than more massive ones (see bottom-right panel in Fig. 5). Naively speaking, it is expected that as galaxies build up their stellar masses, they can provide deeper

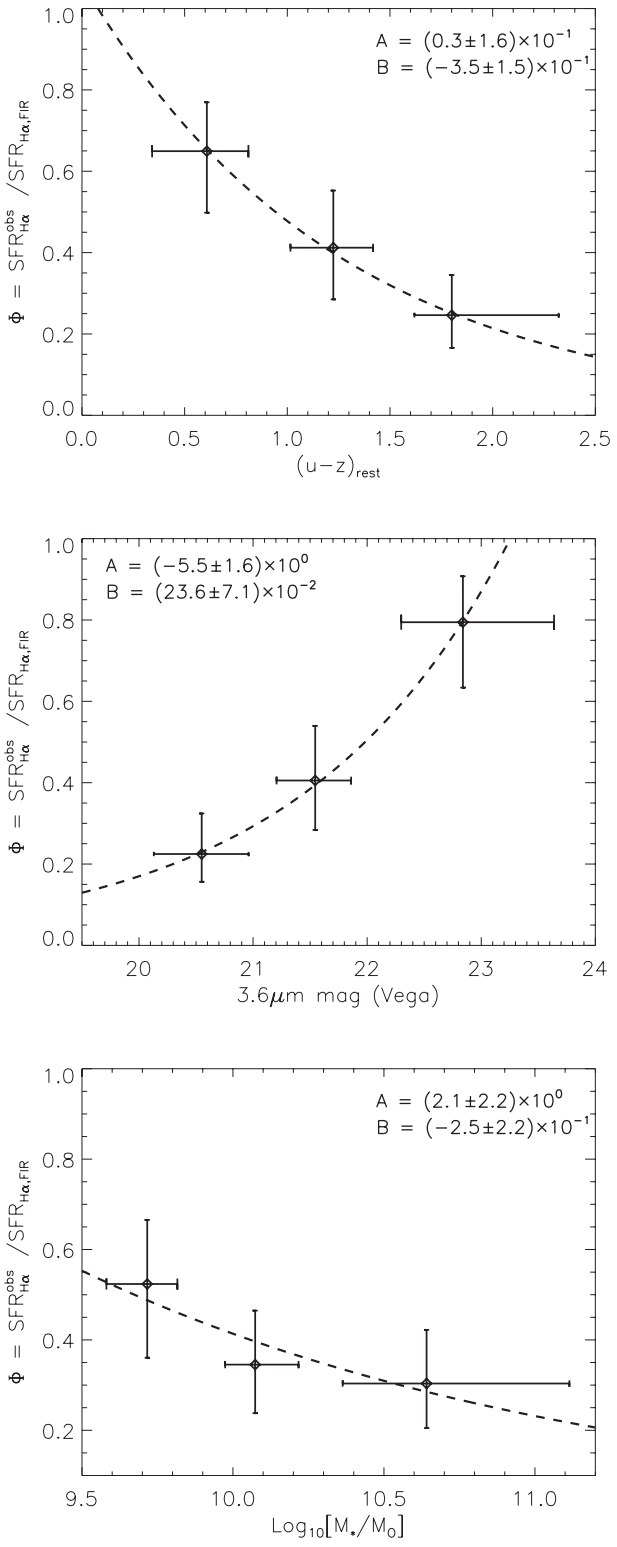

Figure 7. The figures show the parameter Φ, which defines the dominant SFR component – the observed Hα or L(8–1000 μm) luminosity – as a function of rest-frame ($u - z$) colour, observed *Spitzer*-3.6-μm magnitude and stellar mass. This parametrization is presented in Section 4.1.1 and can be used to aid the common lack of the obscured (or unobscured) SFR tracers in high-z galaxies. The inset values at the top of each figure correspond to a simple linear fit, $\log_{10}(\Phi) = A + B \times X$, as presented in equation (6).

potential wells which could then help retain their enriched gas (feedback from star formation activity) and provide dense environments where colossal numbers of stars can rapidly form. Under this assumption, we would expect that massive galaxies would tend to have higher metallicities that can facilitate the creation of a significant amount of dust which cannot escape from the galaxy system, implying typically higher optical depths around star-forming regions. This might be a fundamental reason to explain the increasing component of heavily extinguished star formation in more massive galaxies.

We find that the $A_{\rm H\alpha}(M_*)$ relation presented by Garn & Best (2010) seems to have little or no evolution up to $z = 1.47$, a result that confirms previous analyses by Sobral et al. (2012) and Stott et al. (2013). This put important constraints on the cosmic evolution of the dust properties up to $z = 1.47$, and suggests that the metal enrichment and the dust covering factors do not evolve significantly as a function of redshift. We stress that this correlation is proved using galaxies with $M_* \gtrsim 10^{9.5}$ M$_\odot$, so a vast number of galaxies are excluded in this particular analysis – especially those biased towards high sSFRs. Actually, HiZELS galaxies that do have stellar mass estimates are on average more far-IR luminous than the others. We show this behaviour in Fig. 7, where we present the parameter Φ, which shows the dominant SFR tracer (observed Hα or far-IR luminosity), as a function of rest-frame ($u - z$) colour, 3.6 μm and M_*. We observe that Φ is always $\lesssim$0.5, i.e. those galaxies with available stellar mass estimates are in general dominated by obscured star formation rather than unextinguished Hα.

It is important to note that stellar masses are derived from an SED fit to the rest-frame UV to near-IR photometry, taking into account five main assumptions: metallicity, age, IMF, reddening and star formation history (see Section 3.6). The correlation between this SED-derived SFR and the one derived using the far-IR luminosity is known to present a large scatter (Buat et al. 2010; Wijesinghe et al. 2011), so stellar masses should be used with caution, especially for the most obscured galaxies where the UV could be underestimating the more heavily obscured star-forming regions (see da Cunha, Charlot & Elbaz 2008). We have tried to minimize this bias by introducing an SED coverage right up to the rest-frame near-IR bands to make the SED fit not critically dependent upon rest-frame UV colour (i.e. minimizing changes in the mass-to-light ratio).

The significance of the linear fit's slopes shown in Figs 5 and 6 suggests that $A_{\rm H\alpha}$ has a slightly stronger correlation with *Spitzer*-3.6-μm magnitude than with stellar mass (Figs 5 and 6). This is likely to be because, although the *Spitzer*-3.6-μm magnitude can be used as a broad stellar mass estimator, it also has some sensitivity to young stars from recent star formation.

4.3 HiZELS on the main sequence

In Fig. 8, we compare the sSFR using three different methods: based on the SFR derived from using a combination of Hα and far-IR luminosity (Kennicutt et al. 2009); based on that derived using the far-IR only (Kennicutt 1998); and based on the optically derived SFR using $A_{\rm H\alpha}(M_*)$ (see definitions in Table 3). We find that roughly all sSFR estimates agree, and our preferred SFR$_{\rm H\alpha,\,FIR}$ estimate unsurprisingly lies between the other two predictions. All estimators broadly agree within the errors, although slight discrepancies tend to appear at large stellar masses where the far-IR becomes the dominant SFR tracer. These results suggest that assuming a constant SFR, HiZELS galaxies with lower stellar masses ($M_* \sim 10^{9.7}$ M$_\odot$) are five times more efficient in doubling their stellar mass than more massive ones ($M_* \sim 10^{10.7}$ M$_\odot$), in other words, the characteristic time that

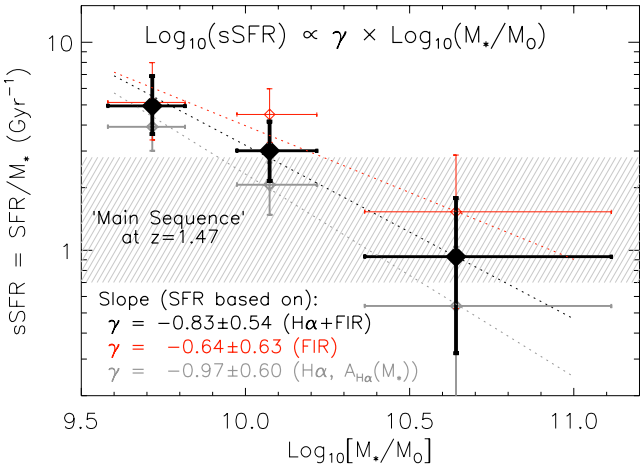

Figure 8. The sSFR (SFR/M_*) for the HiZELS sample at $z = 1.47$ as a function of stellar mass. The thick black and red symbols show the derived sSFR using $SFR_{H\alpha,\,FIR}$ and SFR_{FIR}, respectively (see Table 3). The symbols in light grey are the sSFR derived using intrinsic Hα luminosities counting for extinction using a parametrization of $A_{H\alpha}$ as a function of M_* (Garn & Best 2010, see definition in Table 3). Error bars show the 68 per cent confidence levels. The shaded line filled region shows the 'main sequence' defined in Elbaz et al. (2011) at $z = 1.5$, corrected by a 0.15 dex factor in stellar mass in order to account for the TP-AGB component not included in Elbaz et al.'s analysis (see Section 4.2).

HiZELS galaxies take to double their stellar mass is $\tau \approx 1/5$ Gyr and ≈1 Gyr at low and high M_*, respectively.

The expected sSFR for a 'normal' star-forming galaxy at $z \sim 1.5$ on the main sequence is $1.4^{+1.0}_{-0.5}$ Gyr^{-1}. Note that to be consistent with our analyses, we have decreased the Elbaz et al. (2011) stellar masses by 0.15 dex in order to take into account the TP-AGB component (see Section 3.6). This 'typical' sSFR is slightly lower than the typical value measured for the HiZELS sample (see Fig. 8). As such, the HiZELS sample would be classed as galaxies with a 'starburstiness' value of $R_{BS} = sSFR/sSFR_{MS}(z) \approx 2$ at $z = 1.47$. We note that at this redshift, the range in stellar population is narrower and the Hα contribution from stars that are not related to star formation is likely to be negligible (e.g. Buat et al. 2010).

Taking a look at the characteristic break of the Hα luminosity function at $z \approx 1.47$, $L^*_{H\alpha} = 10^{42.50\pm0.23}$ erg s^{-1} (Sobral et al. 2012), we can confidently say that the HiZELS survey is not identifying the most extreme and rare galaxies, although $L^*_{H\alpha}$ galaxies (which dominate the SFR density) tend to fall in the starburst regime under the Elbaz et al. (2011) definition. As starburst galaxies are only a small fraction in Elbaz et al.'s studies, this might suggest that typical Hα emitters (usually not heavily obscured compared to a far-IR selected sample; $A_{H\alpha} \lesssim 2$) are not included in their work due to selection effects. As most of the HiZELS galaxies have similar properties to the 'normal' ones which define the local Kennicutt et al. (2009) SFR relations (i.e. allowing reliable SFR estimates), we suggest the main sequence might be only valid for those star-forming galaxies which are preferentially obscured (far-IR selected). It suggests that we cannot easily compare our results with previous studies which declare 'star-forming' galaxies to be simply those detected in the far-IR.

It is important to highlight the systematic deviation from the so-called main sequence for star-forming galaxies (Elbaz et al. 2011) at low stellar masses. This is mostly due to a selection effect introduced by the detectability of Hα in the HiZELS survey. Basically, Fig. 8 does not include the faint Hα population composed by a large number of low-mass dwarf galaxies, and in lower number those which are heavily obscured. The most 'starbusty' ones are selected in this work (especially at small stellar masses), implying that HiZELS is only sensitive to 'main-sequence' galaxies at high stellar masses ($M_* \gtrsim 10^{10.2}$ M$_\odot$).

5 CONCLUSIONS

This work provides for the first time a detailed statistical description of the far-IR SED for a uniform sample of 443 Hα-selected star-forming galaxies at $z = 1.47$. The sources are selected from the HiZELS coverage in the UDS and COSMOS fields, and the measured far-IR properties are obtained from *Spitzer* (24, 70 μm), *Herschel* (100, 160, 250, 350 and 500 μm) and AzTEC (1100 μm) images.

We find that the sample of HiZELS galaxies (after removing possible AGN) have a median far-IR luminosity of $L(8-1000\,\mu m) = 10^{11.41^{+0.04}_{-0.06}}$ L$_\odot$, i.e. they are typical LIRGs at $z = 1.47$ presenting $SFR_{H\alpha,\,FIR} = 32 \pm 5$ M$_\odot$ yr^{-1}. Our results have been possible to achieve thanks to a stacking analysis given that these galaxies are generally beneath the noise levels of present far-IR images. In particular, only 2 per cent of the sample is directly detected by *Herschel* at 250 μm, a population composed by massive and heavily obscured galaxies with far-IR luminosities of $\sim 10^{12.1}$ L$_\odot$.

We measure a typical Hα extinction of $A_{H\alpha} = 1.0 \pm 0.2$ mag for the full HiZELS sample at $z = 1.47$, in excellent agreement with typical extinctions seen locally (Garn & Best 2010) and at high-z (Sobral et al. 2012; Stott et al. 2013). We find little or no evolution up to $z = 1.47$ for the correlation between stellar mass and Hα extinction proposed by Garn & Best (2010). These results suggest that the dust properties do not change considerably within this redshift range, giving important constraints on the cosmic evolution of the dust covering factors and the properties of metallicity enrichment.

We find that HiZELS galaxies tend to deviate from the 'main sequence' for star-forming galaxies. This is mostly due to a selection effect given that only the most starbusty ones are above the Hα threshold, especially at low stellar masses. We find that the inclusion of far-IR data to obtain better SFR estimates becomes especially important at high stellar masses.

Our large Hα sample has allowed us to explore a large part of parameter space. In particular, we are able to find a clear correlation between the far-IR luminosity on rest-frame $u-z$ colour and *Spitzer*-3.6-μm fluxes. We find that in HiZELS galaxies presenting red optical $(u - z)_{rest} \lesssim 0.9$ colours or faint 3.6-μm fluxes ($\gtrsim 22$ mag, Vega), the observed Hα luminosity becomes the dominant SFR tracer (rather than far-IR luminosity). We use these dependences to propose a recipe to precisely estimate the SFR in cases where far-IR data are absent in these high-redshift galaxies (see equation 5). This alternative parametrization is valid for samples with $L(H\alpha)_{obs}/L(8-1000\,\mu m) \approx 2/1000$, i.e. when both obscured and unobscured components have similar contributions to the total SFR.

ACKNOWLEDGEMENTS

We thank the anonymous referee for the useful comments that helped improve this paper. EI agradece el financiamento de CONICYT/ FONDECYT por el proyecto de postdoctorado N°:3130504. DS acknowledges financial support from the Netherland Organization for Scientific research (NWO) through a Veni fellowship. IS acknowledges support from STFC, a Leverhulme Fellowship,

the ERC Advanced Investigator programme DUSTYGAL and a Royal Society/Wolfson Merit Award. RJI acknowledges support in the form of ERC Advanced Investigator programme, COSMICISM. The HiZELS data are based on observations obtained using both the Wide Field Camera on the 3.8-m United Kingdom Infrared Telescope (operated by the Joint Astronomy Centre on behalf of the Science and Technology Facilities Council of the UK) and Suprime-Cam on the 8.2-m *Subaru* Telescope, which is operated by the National Astronomical Observatory of Japan. This research has made use of data from the HerMES project (http://hermes.sussex.ac.uk/). HerMES is a *Herschel* Key Programme utilizing Guaranteed Time from the SPIRE instrument team, ESAC scientists and a mission scientist. The data presented in this paper will be released through the HerMES database in Marseille, HeDaM (http://hedam.oamp.fr/HerMES). SPIRE has been developed by a consortium of institutes led by Cardiff Univ. (UK) and including: Univ. Lethbridge (Canada); NAOC (China); CEA, LAM (France); IFSI, Univ. Padua (Italy); IAC (Spain); Stockholm Observatory (Sweden); Imperial College London, RAL, UCL-MSSL, UKATC, Univ. Sussex (UK); and Caltech, JPL, NHSC, Univ. Colorado (USA). This development has been supported by national funding agencies: CSA (Canada); NAOC (China); CEA, CNES, CNRS (France); ASI (Italy); MCINN (Spain); SNSB (Sweden); STFC, UKSA (UK); and NASA (USA). PACS has been developed by a consortium of institutes led by MPE (Germany) and including UVIE (Austria); KUL, CSL, IMEC (Belgium); CEA, OAMP (France); MPIA (Germany); IFSI, OAP/AOT, OAA/CAISMI, LENS, SISSA (Italy); IAC (Spain). This development has been supported by the funding agencies BMVIT (Austria), ESA-PRODEX (Belgium), CEA/CNES (France), DLR (Germany), ASI (Italy) and CICYT/MCYT (Spain). This research has made use of the NASA/IPAC Infrared Science Archive, which is operated by the Jet Propulsion Laboratory, California Institute of Technology, under contract with NASA. This work is based in part on observations made with the *Spitzer* Space Telescope, which is operated by the Jet Propulsion Laboratory, California Institute of Technology under a contract with NASA.

REFERENCES

Amblard A. et al., 2010, A&A, 518, L9
Austermann J. E. et al., 2010, MNRAS, 401, 160
Béthermin M., Dole H., Cousin M., Bavouzet N., 2010, A&A, 516, A43
Béthermin M., Doré O., Lagache G., 2012a, A&A, 537, L5
Béthermin M. et al., 2012b, A&A, 542, A58
Brinchmann J., Charlot S., White S. D. M., Tremonti C., Kauffmann G., Heckman T., Brinkmann J., 2004, MNRAS, 351, 1151
Brocklehurst M., 1971, MNRAS, 153, 471
Bruzual G., 2007, in Vallenari A., Tantalo R., Portinari L., Moretti A., eds, ASP Conf. Ser. Vol. 374, From Stars to Galaxies: Building the Pieces to Build Up the Universe. Astron. Soc. Pac., San Francisco, p. 303
Bruzual G., Charlot S., 2003, MNRAS, 344, 1000
Buat V. et al., 2010, MNRAS, 409, L1
Calzetti D., 2001, PASP, 113, 1449
Cappelluti N. et al., 2009, A&A, 497, 635
Chabrier G., 2003, ApJ, 586, L133
da Cunha E., Charlot S., Elbaz D., 2008, MNRAS, 388, 1595
Daddi E., Cimatti A., Renzini A., Fontana A., Mignoli M., Pozzetti L., Tozzi P., Zamorani G., 2004, ApJ, 617, 746
Daddi E. et al., 2007, ApJ, 670, 156
Daddi E. et al., 2010, ApJ, 714, L118
Dickinson M., Papovich C., Ferguson H. C., Budavári T., 2003, ApJ, 587, 25
Dominguez A. et al., 2013, ApJ, 763, 145
Dunne L. et al., 2011, MNRAS, 417, 1510
Dutton A. A., van den Bosch F. C., Dekel A., 2010, MNRAS, 405, 1690
Elbaz D. et al., 2007, A&A, 468, 33
Elbaz D. et al., 2011, A&A, 533, A119
Fischera J., Dopita M., 2005, ApJ, 619, 340
Frayer D. T. et al., 2009, AJ, 138, 1261
Garn T., Best P. N., 2010, MNRAS, 409, 421
Garn T. et al., 2010, MNRAS, 402, 2017
Geach J. E., Smail I., Best P. N., Kurk J., Casali M., Ivison R. J., Coppin K., 2008, MNRAS, 388, 1473
Geach J. E., Sobral D., Hickox R. C., Wake D. A., Smail I., Best P. N., Baugh C. M., Stott J. P., 2012, MNRAS, 426, 679
Gilbank D. G., Baldry I. K., Balogh M. L., Glazebrook K., Bower R. G., 2010, MNRAS, 405, 2594
Griffin M. J. et al., 2010, A&A, 518, L3
Hayashi M., Sobral D., Best P. N., Smail I., Kodama T., 2013, MNRAS, 430, 1042
Heinis S. et al., 2013, MNRAS, 429, 1113
Hilton M. et al., 2012, MNRAS, 425, 540
Hopkins A. M., Beacom J. F., 2006, ApJ, 651, 142
Hopkins A. M. et al., 2003, ApJ, 599, 971
Hwang H. S. et al., 2010, MNRAS, 409, 75
Ibar E. et al., 2008, MNRAS, 386, 953
Ibar E. et al., 2010, MNRAS, 409, 38
Iglesias-Páramo J. et al., 2006, ApJS, 164, 38
Ivison R. J. et al., 2010a, A&A, 518, L31
Ivison R. J. et al., 2010b, A&A, 518, L35
Karim A. et al., 2011, ApJ, 730, 61
Kennicutt R. C., Jr, 1998, ARA&A, 36, 189
Kennicutt R. C., Jr et al., 2009, ApJ, 703, 1672
Kurczynski P., Gawiser E., 2010, AJ, 139, 1592
Lacki B. C., Thompson T. A., Quataert E., 2010, ApJ, 717, 1
Lacy M. et al., 2004, ApJS, 154, 166
Lawrence A. et al., 2007, MNRAS, 379, 1599
Le Floc'h E. et al., 2009, ApJ, 703, 222
Levenson L. et al., 2010, MNRAS, 409, 83
Lutz D. et al., 2011, A&A, 532, A90
Markwardt C. B. et al., 2009, in Bohlender D. A., Durand D., Dowler P., eds, Astron. Soc. Pac. Conf. Ser., Vol. 411, Astronomical Data Analysis Software and Systems XVIII. Astron. Soc. Pac., San Francisco, p. 251
Moustakas J., Kennicutt R. C., Jr, Tremonti C. A., 2006, ApJ, 642, 775
Niklas S., Klein U., Wielebinski R., 1997, A&A, 322, 19
Noeske K. G. et al., 2007, ApJ, 660, L43
Oliver S. J. et al., 2012, MNRAS, 424, 1614
Pannella M. et al., 2009, ApJ, 698, L116
Pilbratt G. L. et al., 2010, A&A, 518, L1
Poglitsch A. et al., 2010, A&A, 518, L2
Rieke G. H. et al., 2004, ApJS, 154, 25
Rieke G. H., Alonso-Herrero A., Weiner B. J., Pérez-González P. G., Blaylock M., Donley J. L., Marcillac D., 2009, ApJ, 692, 556
Roseboom I. G. et al., 2012, MNRAS, 426, 1782
Salim S. et al., 2009, ApJ, 700, 161
Salpeter E. E., 1955, ApJ, 121, 161
Sanders D. B. et al., 2007, ApJS, 172, 86
Schinnerer E. et al., 2010, ApJS, 188, 384
Scott K. S. et al., 2008, MNRAS, 385, 2225
Scoville N., 2007, in Baker A. J., Glenn J., Harris A. I., Mangum J. G., Yun M. S., eds, ASP Conf. Ser. Vol. 375, From Z-Machines to ALMA: (Sub)Millimeter Spectroscopy of Galaxies. Astron. Soc. Pac., San Francisco, p. 166
Seki J., Yamamoto T., 1980, Ap&SS, 72, 79
Shetty R., Kauffmann J., Schnee S., Goodman A. A., 2009, ApJ, 696, 676
Siebenmorgen R., Krügel E., 2007, A&A, 461, 445
Silva L., Granato G. L., Bressan A., Danese L., 1998, ApJ, 509, 103
Smith A. J. et al., 2012, MNRAS, 419, 377
Sobral D. et al., 2009, MNRAS, 398, 75

Sobral D., Best P. N., Geach J. E., Smail I., Cirasuolo M., Garn T., Dalton G. B., Kurk J., 2010, MNRAS, 404, 1551
Sobral D., Best P. N., Smail I., Geach J. E., Cirasuolo M., Garn T., Dalton G. B., 2011, MNRAS, 411, 675
Sobral D., Best P. N., Matsuda Y., Smail I., Geach J. E., Cirasuolo M., 2012, MNRAS, 420, 1926
Sobral D., Smail I., Best P. N., Geach J. E., Matsuda Y., Stott J. P., Cirasuolo M., Kurk J., 2013, MNRAS, 428, 1128
Stansberry J. A., Grundy W. M., Margot J. L., Cruikshank D. P., Emery J. P., Rieke G. H., Trilling D. E., 2006, ApJ, 643, 556
Stern D. et al., 2005, ApJ, 631, 163
Stott J. P., Sobral D., Smail I., Bower R., Best P. N., Geach J. E., 2013, MNRAS, 430, 1158
Surace J. A., Shupe D. L., Fang F., Evans T., Alexov A., Frayer D., Lonsdale C. J., SWIRE Team, 2005, BAAS, 37, 1246
Swinyard B. M. et al., 2010, A&A, 518, L4
Symeonidis M., Page M. J., Seymour N., Dwelly T., Coppin K., McHardy I., Rieke G. H., Huynh M., 2009, MNRAS, 397, 1728
Symeonidis M. et al., 2011, MNRAS, 417, 2239
Trujillo I., Conselice C. J., Bundy K., Cooper M. C., Eisenhardt P., Ellis R. S., 2007, MNRAS, 382, 109
Ueda Y. et al., 2008, ApJS, 179, 124
Villar V., Gallego J., Pérez-González P. G., Pascual S., Noeske K., Koo D. C., Barro G., Zamorano J., 2008, ApJ, 677, 169
Villar V., Gallego J., Pérez-González P. G., Barro G., Zamorano J., Noeske K., Koo D. C., 2011, ApJ, 740, 47
Wang L. et al., 2013, MNRAS, 431, 648
Wijesinghe D. B. et al., 2011, MNRAS, 415, 1002
Wilson G. W. et al., 2008, MNRAS, 386, 807
Wuyts S. et al., 2011, ApJ, 742, 96
York D. G. et al., 2000, AJ, 120, 1579

This paper has been typeset from a TEX/LATEX file prepared by the author.